Nondegenerate Parametric Amplifiers Based on Dispersion-Engineered Josephson-Junction Arrays

Patrick Winkel, Ivan Takmakov, Dennis Rieger, Luca Planat, Wiebke Guichard, Lukas Grünhaupt, Nataliya Maleeva, Farshad Foroughi, Fabio Henriques, Kiril Borisov, et al.

Nondegenerate Parametric Amplifiers Based on Dispersion-Engineered Josephson-Junction Arrays

Patrick Winkel,[1] Ivan Takmakov,[1,2,3] Dennis Rieger,[1] Luca Planat,[4] Wiebke Hasch-Guichard,[4] Lukas Grünhaupt,[1] Nataliya Maleeva,[1] Farshad Foroughi,[4] Fabio Henriques,[1] Kiril Borisov,[2] Julian Ferrero,[1] Alexey V. Ustinov,[1,3] Wolfgang Wernsdorfer,[1,2,4] Nicolas Roch,[4,*] and Ioan M. Pop[1,2,†]

[1] *Physikalisches Institut, Karlsruhe Institute of Technology, 76131 Karlsruhe, Germany*
[2] *Institute of Nanotechnology, Karlsruhe Institute of Technology, 76344 Eggenstein-Leopoldshafen, Germany*
[3] *Russian Quantum Center, National University of Science and Technology MISIS, 119049 Moscow, Russia*
[4] *Univ. Grenoble Alpes, CNRS, Grenoble INP, Institut Néel, 38000 Grenoble, France*

(Received 23 September 2019; accepted 20 December 2019; published 7 February 2020)

Determining the state of a qubit on a time scale much shorter than its relaxation time is an essential requirement for quantum information processing. With the aid of a nondegenerate parametric amplifier, we demonstrate the continuous detection of quantum jumps of a transmon qubit with 90% fidelity of state discrimination. Entirely fabricated by standard two-step optical-lithography techniques, this type of parametric amplifier consists of a dispersion-engineered Josephson-junction (JJ) array. By using long arrays, containing 10^3 JJs, we can obtain amplification in multiple eigenmodes with frequencies below 10 GHz, which is the typical range for qubit readout. Moreover, if a moderate flux tunability of each mode is introduced, employing superconducting-quantum-interference-device junctions, a single amplifier device could potentially cover the entire frequency band between 1 and 10 GHz.

DOI: 10.1103/PhysRevApplied.13.024015

I. INTRODUCTION

Low-noise microwave amplifiers constitute an essential prerequisite for the implementation of fast high-fidelity quantum-state detection [1–6] in quantum information processing with superconducting quantum bits (qubits) dispersively coupled to readout resonators [7,8]. Although in principle the strength of the readout signal can be increased well above the noise of commercial high-electron-mobility-transistor (HEMT) amplifiers, this typically results in an increase in the energy relaxation rate of the qubits [9,10], which degrades the readout fidelity overall. Over the last decade, this limitation on the signal-to-noise ratio has been successfully overcome thanks to the development of superconducting parametric amplifiers [11–18] which add less noise, down to the quantum limit [19].

In superconducting parametric amplifiers, the nonlinearity required to transfer energy from a strong classical pump tone to a weak quantum signal [20,21] is provided by low-loss inductive elements, namely Josephson junctions (JJs) [22–24], or thin films of a disordered superconductor with an intrinsically high kinetic inductance [25–27]. These nonlinear elements are embedded either in a resonant tank circuit [28] or in a dispersion-engineered microwave transmission line [29–33]. In the first case, amplification occurs only in the vicinity of the standing-wave eigenfrequency of the circuit, while in the case of traveling-wave parametric amplifiers, the tones applied interact during propagation along the transmission line in a much larger frequency band, covering several gigahertz.

Ideally, a parametric amplifier offers a signal power gain $G \geq 20$ dB in a frequency band larger than the linewidth of the readout resonator, a saturation power well above the single-photon regime [34–40], and isolation of the qubit-resonator system from the strong pump [41–43]. Although there has been impressive progress in the development of broadband traveling-wave parametric amplifiers [29–33], optimizing these figures of merit for a specific application is generally simpler for a standing-wave parametric amplifier.

We present a standing-wave parametric-amplifier design based on superconducting-quantum-interference-device (SQUID) arrays containing up to 1800 SQUIDs, with an engineered dispersion relation realizing pairs of hybridized modes (dimers) suitable for nondegenerate parametric amplification (see Fig. 1). By applying a strong, single-frequency pump tone between the hybridized modes, we demonstrate signal power gains exceeding 20 dB for up to four dimers in a single device (see Fig. 2), over an instantaneous bandwidth between 5 and 15 MHz. The

*nicolas.roch@neel.cnrs.fr
†ioan.pop@kit.edu

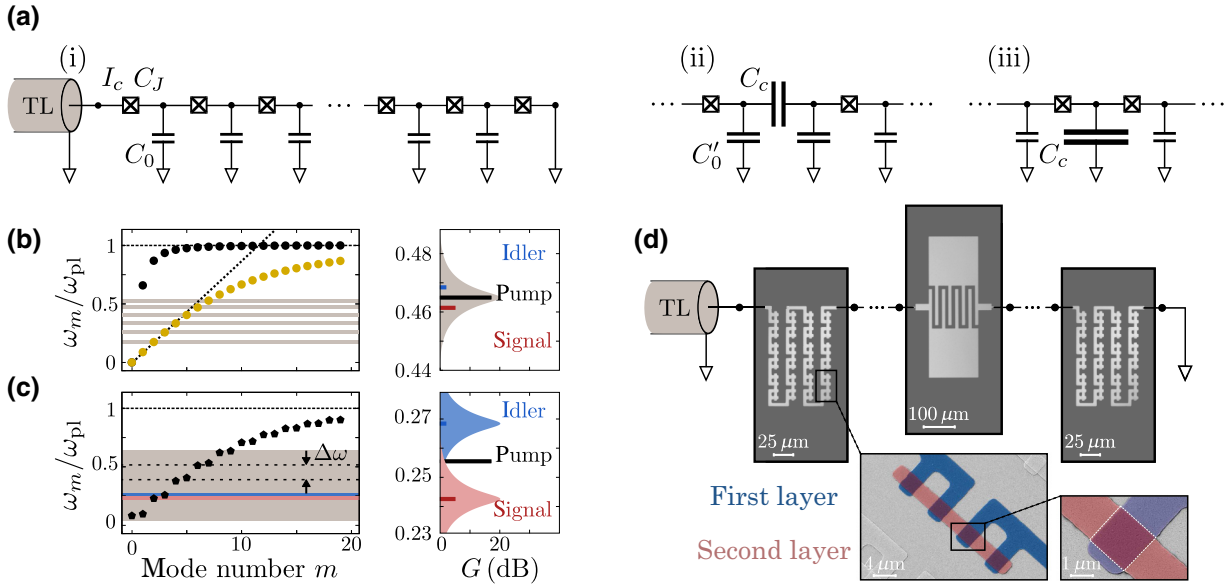

FIG. 1. Dispersion engineering and optical-lithography implementation of a JJ array. (a) Schematic circuit diagram of a Josephson-junction array resonator. The array consists of N identical dc SQUIDs in series (for simplicity shown here as single boxes) with a Josephson energy $E_J = \Phi_0 I_c/2\pi$ and charging energy $E_c = e^2/2C_J$. The JJs are connected by superconducting islands with a capacitance to ground C_0. (i) The array is galvanically coupled to a 50-Ω on-chip transmission line and terminated to ground at the other end. We engineer the dispersion relation by introducing a capacitance C_c in the center of the array, either (ii) in series with C_J or (iii) in parallel with C_0. (b) Calculated dispersion relation of a short ($N = 180$ JJs, black) and a long ($N = 1800$ JJs, yellow) JJ-array resonator for a typical value $C_J/C_0 = 2500$. The eigenfrequencies ω_m are normalized to the plasma frequency $\omega_{pl} = \sqrt{8E_J E_c}$. For the short array, only a single physical mode is in the linear regime of the dispersion relation, while the rest of the eigenmodes accumulate near ω_{pl}. When the length of the array is increased, the dispersion relation flattens and several eigenmodes populate the linear regime, which is indicated by the black dotted line. (c) Eigenmode spectrum of a long JJ-array resonator ($N = 1800$ JJs) engineered according to panel (ii) or (iii). Because of the center capacitance, pairs of neighboring modes hybridize, forming a dimer each. The frequency splitting between dimer modes, $2J_n$, depends on the mode number n and the value of C_c, among other things, and we design it to be comparable to the mode linewidth κ_n, in the range of several hundreds of megahertz. As indicated in the right-hand panels, each individual mode can be used for degenerate amplification, while each dimer is suitable for nondegenerate amplification. (d) Optical-microscope images of various sections of the JJ array, including the interdigitated capacitor C_c in the center. The array consists of optically fabricated dc SQUIDs on a sapphire substrate arranged in a meander structure comprising six SQUIDs per meander. The area of the SQUID loop is $A_L \approx 4 \times 4\ \mu\text{m}^2$. The false-colored scanning-electron-microscope (SEM) images in the bottom panels depict two neighboring SQUIDs and a single JJ. We highlight the first aluminum layer in blue and the second in red. From the measured junction area $A_J \approx 3.1 \times 3.2\ \mu\text{m}^2$, we estimate a junction capacitance $C_J \approx 500$ fF.

pump-tone frequency is detuned from the signal by hundreds of megahertz, which enables its filtering. We refer to these devices as dimer Josephson-junction-array amplifiers (DJJAAs). We note that a similar idea was developed in parallel in Ref. [44], where several modes of SNAIL [45] (superconducting nonlinear asymmetric inductive element) arrays were used for amplification.

This paper is organized as follows. In Sec. II, we present the DJJAA concept, followed by the effective circuit model in Sec. III, which is used to calculate the dispersion relation, eigenfunctions, and first-order nonlinear coefficients of the DJJAA. In Sec. IV, we describe the optical-fabrication process. In Sec. V, we show power-gain measurements for three DJJAAs. For the longest array investigated (1800 SQUIDs), we observe nondegenerate amplification exceeding 20 dB for four individual dimers in a single DJJAA device, epitomizing the potential of this amplifier design. Section VI is devoted to noise characterization. Using an array of 1200 SQUIDs, we calibrate the measurement efficiency η of our setup [46] by observing quantum jumps of a transmon qubit [47]. We find $\eta \approx 0.13$ for the whole setup and $\eta_{\text{DJJAA}} \geq 0.26$ for our parametric amplifier, which is comparable to values reported in the literature [31,46,48]. In Sec. VII, we conclude by summarizing the main results.

II. CONCEPT

The eigenmode spectrum of a Josephson-junction array (JJA) [see Fig. 1(a)] contains N eigenmodes, given by the total number of JJs [40,49–53]. For small frequencies, the effective wavelength of the eigenmodes is much larger than the distance between neighboring JJs, and the mode frequency increases almost linearly with the mode

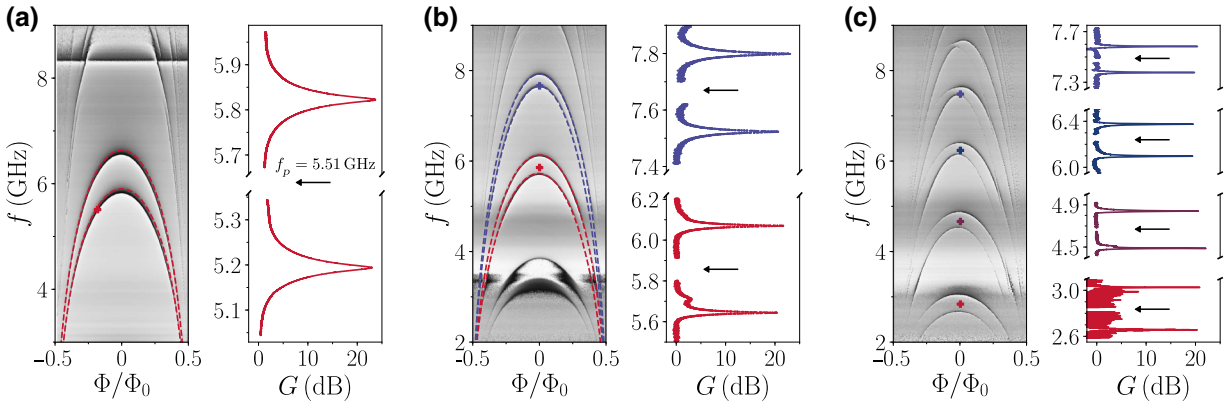

FIG. 2. Phase response of the complex reflection coefficient $\arg(S_{11})$ measured as a function of the probe frequency f and the externally applied flux Φ for three dispersion-engineered JJ arrays: (a) $N = 1200$ JJs, $I_c \approx 6.0$ μA, $C_c = 30$ fF; (b) $N = 1600$ JJs, $I_c \approx 3.0$ μA, $C_c = 40$ fF; (c) $N = 1800$ JJs, $I_c \approx 2.3$ μA, $C_c = 45$ fF. The dispersion relation is dimerized by introducing C_c in series with C_J in the center of the array [see panel (ii) in Fig. 1(a)]. For all plots, the color scale covers the entire range from $-\pi$ (black) to π (white). In (a) and (b) we show with dashed lines a typical example of numerical fits to the eigenmodes, used to calibrate the magnetic-coil current and to extract the device parameters. As expected, the number of modes within a given frequency range (in our case 4–8 GHz) increases with increasing N and decreasing I_c. When a strong pump tone between two hybridized modes is applied, nondegenerate power gain exceeding $G_0 = 20$ dB is observed for up to four pairs of modes in a single device, as shown in panel (c). The arrow and cross symbols in each panel indicate the external flux bias Φ and pump frequency f_p, respectively, color-coded for each dimer. The horizontal features visible in the vicinity of 4 and 8 GHz correspond to the frequency band of the circulator attached to the DJJAA input port.

index m [see Fig. 1(b)]. The slope of this linear regime is determined by the square root of the ratio between the capacitance per unit length arising from the junction capacitance C_J, and the capacitance to ground C_0 [54]. When the effective wavelength of the eigenmodes becomes comparable to the distance between the JJs, the dispersion relation becomes nonlinear, eventually saturating at the self-resonance frequency of a single JJ, referred to as the plasma frequency, $\omega_{\rm pl} \approx 1/\sqrt{L_J C_J}$. Here, L_J is the junction inductance, C_J is the junction capacitance, and we neglect the contribution of C_0. Because of the nonlinearity of the JJ cosine potential, each eigenmode is itself nonlinear in power. As we show in the following, this nonlinearity can be used for parametric amplification.

In general, parametric amplifiers are classified into degenerate and nondegenerate designs, depending on whether the signal (ω_s) and idler (ω_i) tones occupy the same or different physical modes [28]. In the latter case, protecting the quantum circuit under investigation from the influence of the strong pump tone becomes considerably simpler, since the signal and pump tones are detuned in frequency.

In order to obtain nondegenerate amplification, we introduce a capacitor into the center of the JJ array, which, depending on the design [see Fig. 1(a), panels (ii) and (iii)], either splits the array into two capacitively coupled sections or capacitively shunts the central island to the ground. In either of these cases, the capacitor breaks the symmetry between even and odd modes, and creates pairs of hybridized modes [see Fig. 1(c)]. Each pair, referred to as a dimer in the following, is suitable for nondegenerate parametric amplification by applying a pump tone between the two modes. In this four-wave-mixing process, two pump photons are converted into a signal and an idler photon ($\omega_s + \omega_i = 2\omega_p$, where ω_p is the pump frequency), similarly to the scheme presented in Ref. [18]. The device works in reflection, with the pump added to the signal.

The intrinsic limitation on the instantaneous bandwidth for standing-wave parametric amplifiers is overcome by employing SQUID junctions with a flux-tunable critical current $I_c(\Phi)$. Tuning the device frequency by lowering I_c also increases the impact of higher-order nonlinear terms arising from the Josephson potential, which eventually limits the amplifier performance in terms of dynamic range [36–38] and therefore bounds the tuning bandwidth. In order to mitigate the effect of higher-order terms and maximize the saturation power of the device, we use long arrays of JJs similar to the approaches in Refs. [12,34,35,40,55,56].

The tunable bandwidth of the DJJAA is given by the flux tunability of each dimer suitable for amplification. Since the frequency difference $\Delta\omega$ between neighboring dimers decreases as the number of SQUIDs is increased [see Fig. 1(c)], we can imagine that $\Delta\omega$ can be reduced to values comparable to the flux-tunable bandwidth of each dimer. In this case, the effective tunable bandwidth of the DJJAA would span the entire linear part of the dispersion relation, which is typically several gigahertz wide [highlighted in gray in Fig. 1(c)]. As discussed in Sec. V, we demonstrate a step in this direction by showing a power gain reaching

20 dB for four different dimers in the same device, spread over a frequency range of 4 GHz.

III. CIRCUIT MODEL

In order to calculate the dispersion relation of our DJJAAs, we derive the system Lagrangian from an effective circuit model. The SQUID arrays consist of N SQUIDs in series, with zero-field critical current I_c and junction capacitance C_J, which are connected by superconducting islands with a capacitance C_0 to ground [see panel (i) in Fig. 1(a)]. For simplicity, additional capacitances arising between islands due to long-range Coulomb interactions mediated by the shared ground plane [52] are neglected in our model. The input port of the array is galvanically coupled to a 50-Ω on-chip transmission line, while the other end is terminated to ground. In the center of the array, we introduce an additional capacitance C_c either in series with C_J [see panel (ii) in Fig. 1(a)] or in parallel with C_0 [see panel (iii) in Fig. 1(a)].

Although both options for the dispersion engineering of the array [see panels (ii) and (iii) in Fig. 1(a)] result in dimers which can be used for nondegenerate amplification, we will discuss only the first approach in detail in the following.

Because of the physical dimensions of the center capacitor plates, the capacitance C_0' to ground of the central nodes with indices $N/2$ and $N/2+1$ is enhanced ($C_0' \gg C_0$) in the first case. The Lagrangian of our system can be written as

$$\begin{aligned}\mathcal{L} = &\sum_{i=1}^{N/2-1} \frac{C_0}{2}\dot{\Phi}_i^2 + \sum_{i=N/2+2}^{N} \frac{C_0}{2}\dot{\Phi}_i^2 \\ &+ \frac{C_0'}{2}\left(\dot{\Phi}_{N/2}^2 + \dot{\Phi}_{N/2+1}^2\right) + \frac{C_c}{2}\left(\dot{\Phi}_{N/2+1} - \dot{\Phi}_{N/2}\right)^2 \\ &+ \sum_{i=0}^{N/2-1} \frac{C_J}{2}\left(\dot{\Phi}_{i+1} - \dot{\Phi}_i\right)^2 + \sum_{i=N/2+1}^{N} \frac{C_J}{2}\left(\dot{\Phi}_{i+1} - \dot{\Phi}_i\right)^2 \\ &- \sum_{i=0}^{N/2-1} E_J \cos(\phi_{i+1} - \phi_i) - \sum_{i=N/2+1}^{N} E_J \cos(\phi_{i+1} - \phi_i).\end{aligned} \tag{1}$$

Here, $E_J = \Phi_0 I_c/2\pi$ is the Josephson energy, and ϕ_n is the superconducting phase of the nth island, with the corresponding node flux $\Phi_n = \Phi_0\phi_n/2\pi$. For a system galvanically coupled to the environment at both ends, the boundary conditions are $\Phi_0 = \Phi_{N+1} = 0$.

In the limit of a small circulating current $I \ll I_c$, the phase drop $\phi_{i+1} - \phi_i$ across each JJ is small, and we can describe the JJs as linear inductors with a kinetic inductance $L_J = \Phi_0/2\pi I_c$. By introducing the node-flux vector $\vec{\Phi} = (\Phi_0, \ldots, \Phi_{N+1})$, Eq. (1) can be rewritten in a matrix representation as

$$\mathcal{L} = \frac{1}{2}\dot{\vec{\Phi}}^T\tilde{C}\dot{\vec{\Phi}} - \frac{1}{2}\vec{\Phi}^T\tilde{L}^{-1}\vec{\Phi}, \tag{2}$$

where $\tilde{C}$ and $\tilde{L}$ are the capacitance and inductance matrices, respectively (see Appendix A). Following Eq. (2), the eigenfrequencies ω_m of the system are calculated by numerically solving the eigenvalue problem [51]

$$\tilde{C}^{-1/2}\tilde{L}^{-1}\tilde{C}^{-1/2}\vec{\Psi}_m = \omega_m^2\vec{\Psi}_m, \tag{3}$$

where the corresponding eigenvectors $\vec{\Psi}_m$ are related to the node-flux eigenvectors $\vec{\Phi}_m$, which carry information about the spatial mode distribution along the array [50].

In order to illustrate the effect of increasing the number of SQUIDs N in the array, in Fig. 1(b) we plot the dispersion relation obtained from Eq. (3) for two arrays with $N = 180$ (black) and $N = 1800$ (yellow), while maintaining a fixed ratio $C_J/C_0 = 2500$. For clarity, the eigenfrequencies ω_m are normalized to the plasma frequency ω_{pl}. The longer the chain, the more eigenmodes fall into the linear regime, with a decreasing frequency detuning $\Delta\omega = (\omega_{i+1} - \omega_i)$ between neighboring modes. For the long array (yellow) and assuming a typical plasma frequency $\omega_{pl} \approx 20$ GHz, the eigenmodes falling into the technologically favored frequency range below 10 GHz are highlighted by horizontal gray lines. As indicated by the panel on the right, each eigenmode is suitable for degenerate amplification by applying a pump tone on resonance.

As a result of the introduction of the capacitance C_c in the center of the array according to Fig. 1(a), panel (ii), the system exhibits symmetric and antisymmetric pairs of hybridized modes [see Fig. 1(c)], referred to as dimers. As indicated in the panel on the right, each dimer is suitable for nondegenerate amplification when a single-frequency pump tone is applied through the input port, between the two dimer modes, similarly to the concept presented in Ref. [18]. Because of this off-resonant pumping scheme, the signal frequency ω_s is well detuned from the pump frequency ω_p, reducing pump leakage [9,46,57].

In order to make it possible to couple the pump tone to both dimer modes, the frequency difference $2J_n$ between the two modes of the dimer, where n denotes the dimer index, is designed to be comparable to the linewidth of the amplifier. In our case J_n is on the order of several hundreds of megahertz and depends on the size of the center capacitance C_c and its energy participation ratio in each mode, which is related to the total length of the chain. Therefore, as a rule of thumb, the values of C_c and N are linearly related. From calculations based on Eq. (3), we choose $C_c = 45$ fF and $C_c = 30$ fF for $N = 1800$ and $N = 1200$, respectively. In both cases, using finite-element

simulations of the capacitor geometry [see Fig. 1(d)], we extract a parasitic capacitance to ground $C_0' = 33$ fF.

Starting with the linear circuit model of Eq. (2), we can perturbatively introduce the nonlinearity arising from the Josephson potential by expanding up to the quartic term $\propto \Delta\phi^4$ and applying the rotating-wave approximation [51,52]. We obtain the Hamiltonian

$$\mathbf{H} = \sum_{m=0}^{N-1} \hbar\omega_m \mathbf{a}_m^\dagger \mathbf{a}_m - \sum_{m=0}^{N-1} \frac{\hbar}{2} K_{m,m}\omega_m \mathbf{a}_m^\dagger \mathbf{a}_m \mathbf{a}_m^\dagger \mathbf{a}_m - \sum_{m,k=0}^{N-1} \frac{\hbar}{2} K_{m,k}\omega_m \mathbf{a}_m^\dagger \mathbf{a}_m \mathbf{a}_k^\dagger \mathbf{a}_k, \tag{4}$$

where $\mathbf{a}_m^\dagger$ and $\mathbf{a}_m$ are the bosonic single-mode field-amplitude creation and annihilation operators, while $K_{m,m}$ and $K_{m,k}$ are the self-Kerr and cross-Kerr coefficients, respectively. The first term describes the harmonic system, the second term relates the frequency of the mth mode ω_m to the mean circulating-photon number $\bar{n}_m$ of that same mode, and the third term describes the interaction between two modes with indices m and k. Using the same notation as in Ref. [51], the Kerr coefficients expressed in terms of the circuit parameters are

$$K_{m,m} = \frac{2\hbar\pi^4 E_J \eta_{mmmm}}{\Phi_0^4 C_J^2 \omega_m^2}, \qquad K_{m,k} = \frac{4\hbar\pi^4 E_J \eta_{mmkk}}{\Phi_0^4 C_J^2 \omega_m \omega_k}. \tag{5}$$

Besides the JJ parameters E_J and C_J, the Kerr coefficients depend on the eigenfunctions $\vec{\Phi}_m$, which give the dimensionless factors η_{mmkk} (see Appendix B). It is the Kerr terms which can give rise to parametric amplification under microwave pumping.

IV. DEVICE FABRICATION AND MEASUREMENT SETUP

The SQUID arrays are implemented in a microstrip geometry with a platinum back-surface metallization of thickness $t = 300$ nm, and are arranged in a meander structure comprising six SQUIDs per meander. The minimum feature size is chosen to be relatively large, around 3 μm, in order to facilitate microfabrication using optical-lithography techniques for the entire device. The circuit is patterned in two separate steps, each followed by a zero-angle aluminum (Al) thin-film evaporation, of thicknesses 30 and 40 nm. Before depositing the second Al layer, we apply an *in situ* argon-milling cleaning step to remove the native oxide from the surface of the first Al layer [58,59]. The Al/AlO_x/Al JJs are formed by the overlap areas between the first and the second Al layer, with an area $A_{JJ} \sim 9$–11 μm^2. AlO_x denotes nonstoichiometric insulating aluminum oxide grown under static oxidation in an oxygen pressure of 10 mbar for 2–4 min. Because of the relatively small loop area $A_L \approx 4 \times 4$ μm^2 and wire width $w \approx 3$–4 μm of the SQUID in our design, the inductive contribution of the loop L_{loop} to the flux modulation is negligible ($L_{\text{loop}} \ll L_J$). In addition, each island adds a stray inductance $L_{\text{stray}} \approx 20$–$30$ pH.

The sapphire chips hosting the DJJAAs are glued onto a copper sample holder using silver paste, which has a dedicated superconducting flux coil integrated into the lid (see Appendix F). The on-chip transmission line is connected to the coaxial input port of the sample holder with aluminum microbonds. A microwave circulator is connected directly to the sample-holder port, and is used to separate the incident from the reflected outgoing signal. The DJJAAs are anchored to the millikelvin stage of a dilution refrigerator with a base temperature $T_{\text{base}} \approx 20$–$30$ mK, and probed in a single-port reflection measurement. After reflection from the DJJAA, the outgoing signal is further amplified by two commercial amplifiers, a HEMT amplifier at 4 K and a room-temperature amplifier.

V. GAIN MEASUREMENTS

The left-hand panels in Figs. 2(a)–2(c) show the phase of the complex reflection coefficient $\arg(S_{11})$ as a function of the probe frequency f and the external flux bias Φ for three different samples with total numbers of SQUIDs $N = 1200$, 1600, and 1800. The respective critical currents per SQUID are $I_c = 6.0$ μA, 3.0 μA, and 2.3 μA, with corresponding Josephson inductances $L_J = 55$ pH, 110 pH, and 143 pH, respectively. Because of the sweep in design parameters, we observe a single dimer in (a), three dimers in (b), and four dimers in (c). With increasing external flux, the frequency of the dimers decreases, as expected from the increasing SQUID inductance, with several higher modes becoming visible close to full SQUID frustration ($|\Phi/\Phi_0| \approx 0.5$). The dashed lines depicted for the first two samples indicate numerical fits to estimate the stray inductance L_{stray} of the circuit design and to calibrate the bias current of the superconducting field coils (see Appendix D). Furthermore, from these fits we conclude that the SQUID asymmetry ($I_{c,1} \neq I_{c,2}$) and the loop inductance L_{loop} can be neglected.

The right-hand panels in Figs. 2(a)–2(c) depict the power gain G in decibels as a function of the probe frequency f when an additional pump tone of power P_p and frequency f_p is applied between two dimerized modes. The black arrows and the cross symbols, which are color-coded individually for each dimer, indicate the external bias flux Φ and the pump frequency, respectively, used in each experiment. For all dimers, the pump frequency is off-center with respect to the low-probe-power response, since the mode population $\bar{n}_m$ caused by the

strong pump tone shifts the dimer modes in frequency by an amount $K_{m,m}\bar{n}_m$. The observed power-gain profile in the high-gain limit ($G \gg 1$) is composed of two overlapping Lorentzian curves, symmetrically emerging below and above the pump-tone frequency. Because of the self-Kerr coefficients $K_{m,m}$ [see Eq. (5)], the frequency detuning between the two maxima depends on the pump power and the pump frequency, similarly to Ref. [18]. The power gain exceeds 20 dB, which is a typical value required to saturate the classical noise added by higher-temperature amplifier stages with amplified quantum noise.

As in the case of other Josephson parametric amplifiers (JPAs), there is a compromise between the maximum of the gain, G_0, and the amplifier's instantaneous bandwidth, B, defined as the full width at half maximum (FWHM), which is reflected by a constant gain-bandwidth product $\sqrt{G_0}B$ [21]. For the sample shown in Fig. 2(a), which has the largest coupling, we find $\sqrt{G_0}B \approx 170$ MHz at the flux sweet spot ($\Phi = 0$). This value is in good agreement with the average of the two measured resonator linewidths $\bar{\kappa}/2\pi = 172$ MHz, as expected for two parametrically coupled modes [18,21]. Thanks to the SQUID junctions, the frequency at which we obtain gain is flux tunable. We typically measure a tunable bandwidth of around 1 GHz per dimer (see Appendix H).

The input saturation power $P_{1\,\mathrm{dB}}$, conventionally defined as the signal-probe power at which the maximum power gain G_0 decreases by 1 dB (the 1-dB compression point), reportedly scales with the ratio of the amplifier linewidth and the self-Kerr coefficient $\kappa_n/|K_{n,n}|$ [37,38]. In our case, this ratio depends on the dimer mode number n, in accordance with the corresponding spatial mode distribution $\vec{\Phi}_n$ (see Sec. III). Thanks to the large number of SQUIDs in our design, the self-Kerr coefficients are strongly reduced for the lowest modes of the dispersion relation compared with designs with only a single or a few SQUIDs [15,17]. For this reason, $P_{1\,\mathrm{dB}}$ is found to be enhanced by an order of magnitude in SQUID-array-based amplifiers similar to those in our approach [18,40]. As we describe in the following section, this allows us to operate the DJJAA at a signal strength of $P_s \geq -118$ dBm ($\geq$420 photons $\times\, \mu\mathrm{s}^{-1}$) without observing the onset of saturation.

VI. NOISE CHARACTERIZATION

A. Power calibration

In order to evaluate the noise performance of a typical DJJAA parametric amplifier, we calibrate the signal power referred to its input port with a transmon qubit [47], which is dispersively coupled to a dedicated readout resonator, as shown in Fig. 3. In the close vicinity of the resonance frequency f_r of the readout resonator, the signal strength can be expressed in number of measurement photons n_{meas}

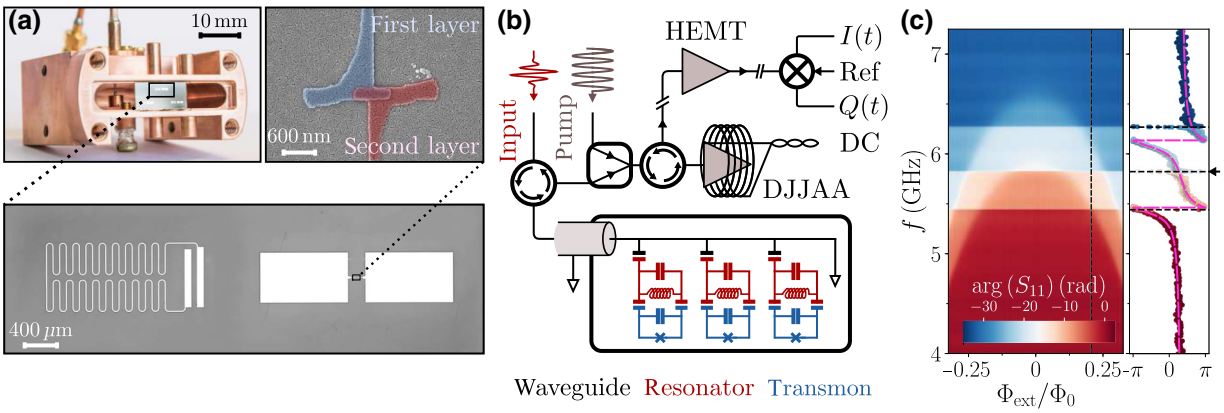

FIG. 3. Transmon qubit samples. (a) Photograph of the copper-waveguide sample holder. In the center of the waveguide, where the electric field is maximum, we place a sapphire chip with three transmon qubits, each capacitively coupled to a dedicated lumped-element readout resonator. The lower panel shows an optical image of one of the transmon qubits and its readout resonator, with an estimated coupling strength $g/2\pi \approx 35$ MHz (see Appendix I). The top right panel depicts a SEM image of a single JJ. All structures are patterned using electron-beam lithography, and are deposited by shadow-angle evaporation. (b) Circuit diagram of the measurement setup. The transmon qubits (blue) are dispersively coupled to the readout resonators (red) and mounted inside the waveguide (black). The readout signal (red arrow) is preamplified by a DJJAA and routed to a commercial HEMT mounted at 4 K. At room temperature, the signal is decomposed into its in-phase and out-of-phase quadratures using a heterodyne microwave interferometer. The DJJAA pump tone (gray arrow) is fed into the signal path through a commercial power combiner. The flux bias for the DJJAA is supplied by an external magnetic-field coil (see Appendix F). (c) Unwrapped phase of the complex reflection coefficient, $\arg(S_{11})$, as a function of frequency f and applied bias flux Φ_{ext} measured from the input port. The three sharp flux-independent phase rolls are due to the readout resonators, and the two broad flux-dependent features are given by an amplifier dimer [see Fig. 2(a)]. The right-hand panel depicts the wrapped phase response along the black dashed line for the DJJAA flux bias used to measure quantum jumps of the transmon coupled to the resonator at $f_r = 5.8224$ GHz (indicated by the black arrow). The pink line indicates a fit to the linear response of the DJJAA (for details, see Appendix G).

[46,48]. In a continuous single-port reflection measurement, the measurement photon number is

$$n_{\text{meas}} \underset{\gamma_r \to 0}{=} \bar{n}_r \frac{\kappa_r}{4} T_m, \tag{6}$$

where T_m is the measurement integration time, $\bar{n}_r$ is the mean number of photons circulating inside the readout resonator, and γ_r and κ_r are the resonator's internal and external decay rates, respectively.

The qubit sample design contains three transmon qubits, each containing a single Josephson junction shunted by an in-plane plate capacitor with rectangular pads, which are capacitively coupled to a dedicated lumped-element readout resonator [see Fig. 3(a)]. The fabrication is based on the bridge-free technique [60], a shadow-angle evaporation technique, and the evaporation of two aluminum thin films on a double-polished sapphire substrate, separated by an oxide barrier.

Each chip is mounted in a 3D-waveguide sample holder [61] [see Fig. 3(a)] and measured in reflection [see Fig. 3(b)]. The reflected readout signal is routed to a DJJAA using a cryogenic circulator. The pump tone, which serves as the power supply for our parametric amplifier, is fed into the signal path with a commercial power combiner. The incident and reflected (amplified) signals are again separated by employing a cryogenic circulator directly mounted at the input of the DJJAA, and subsequently further amplified by two amplifier stages, a commercial HEMT amplifier with a specified noise temperature $T_{N,\text{HEMT}} \approx 2.3$ K, mounted at 4 K, and a room-temperature amplifier, with $T_{N,\text{RT}} \approx 170$ K.

Figure 3(c) depicts the unwrapped phase of the measured complex reflection coefficient $\arg(S_{11})$ in radians as a function of the probe frequency f and external flux Φ_{ext}. The frequencies of the three readout resonators, each coupled to a transmon qubit, are independent of the applied flux bias and are visible as sharp horizontal lines. Since the amplifier modes are much more strongly coupled to the input port than the readout resonators are ($\kappa \gg \kappa_r$), the dimer modes appear as broad features. The right-hand panel depicts the wrapped phase response for the flux bias indicated by the black dashed line in the left-hand panel. For clarity, the readout-resonator frequencies are indicated by horizontal black lines. The dashed pink line indicates the fitted phase response, given by two DJJAA modes separated by $2J/2\pi = 670$ MHz and coupled to the input port with coupling rates $\kappa_+/2\pi = 148$ MHz and $\kappa_-/2\pi = 139$ MHz (see Appendix G for details).

The frequency of the readout resonator ($f_r = 5.8224$ GHz) coupled to the transmon qubit used to calibrate the DJJAA noise (see Sec. VI C) is indicated by the small black arrow on the right-hand side.

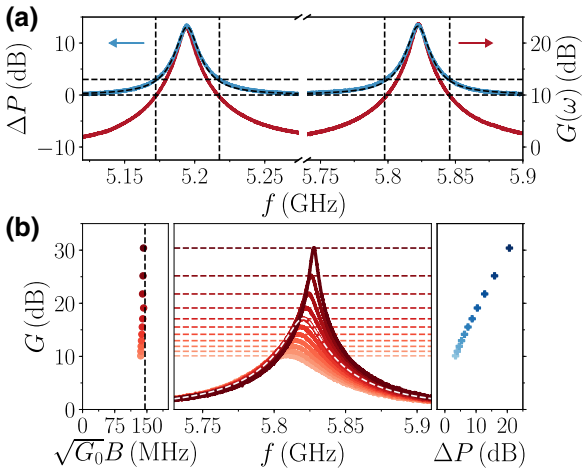

FIG. 4. Noise visibility. (a) Noise visibility ΔP (left axis) and power gain G (right axis) in decibels as a function of frequency for the flux bias and pump power used during the qubit experiments. The maximum power gain $G_0 = 23.2$ dB and corresponding bandwidth (FWHM) $B \approx 9.2$ MHz are extracted from Lorentzian fits. The observed noise visibility at maximum gain is $\Delta P = 14.2$ dB. (b) Power gain G in decibels as a function of frequency for various pump powers. For each curve, G_0 and B are extracted from Lorentzian fits to the amplifier response, generically indicated by the dashed white line (central panel). The calculated gain-bandwidth product $\sqrt{G_0}B \approx 143$ MHz is in good agreement with the theoretical prediction (black line, left panel). For each pump condition, the noise visibility ΔP is measured too, with the visibility at maximum power gain plotted in blue.

B. Noise visibility

During the qubit experiments, we operate our parametric amplifier at a power gain $G_0 = 23.2$ dB and an instantaneous bandwidth $B = 9.2$ MHz, which we extract from individual Lorentzian fits to both lobes [see Fig. 4(a), red line]. By monitoring the output power spectrum with and without the pump tone applied, we observe a maximum noise visibility, i.e., rise in noise compared with the background outside the band, of $\Delta P = 14.2$ dB at the frequency of maximum power gain [see Fig. 4(a), blue line]. This implies that the HEMT noise accounts for only 4% of the room-temperature noise. In Fig. 4(b), we show the measured gain-bandwidth (GB) product $\sqrt{G_0}B$ (see left-hand panel) and noise visibility ΔP (see right-hand panel) at maximum power gain G_0 for various pump strengths. The GB product is in good agreement with the theoretical prediction, indicated by the black dashed line [18].

C. Measurement efficiency

To characterize the measurement efficiency η of the setup, we measure the noise added by the DJJAA by decomposing the output signal into its quadratures $I(t)$ and $Q(t)$. In order to calibrate the measurement photon number n_{meas} [see Eq. (6)] corresponding to the recorded

quadrature voltages, we calibrate the mean number of photons circulating inside the resonator $\bar{n}_r$ by measuring the qubit's fundamental transition frequency f_q in a sequence of Ramsey-fringe experiments [62]. The frequency f_R of the Ramsey oscillations is given by the detuning of the drive from the qubit's transition frequency $f_R = |f_d - f_q|$, which is chosen to be comparable to the frequency shift induced by the population of the readout resonator $\Delta f_q = \bar{n}_r \chi_{qr}$, where $\chi_{qr} = 480$ kHz is the dispersive shift of the qubit [8]. We populate the resonator with $\bar{n}_r$ photons by simultaneously applying a constant tone to the readout resonator at the frequency f_r (see Appendix J).

As shown in Fig. 5, we can now express the histogram of measured signal quadratures $I(t)$ and $Q(t)$ in units of the measurement photon amplitude $\sqrt{n_{\mathrm{meas}}}$, for $\bar{n}_r \approx 150$ and an integration time $T_m = 500$ ns. The qubit's ground state $|g\rangle$ and first excited state $|e\rangle$ are visible as two circles with Gaussian profiles. For clarity, we rotate the I-Q plane such that the information about the qubit state is encoded entirely in the Q quadrature, as shown by the slices through the histogram along I [see top panel in Fig. 5(a)] and Q [see right panel in Fig. 5(a)]. The angle between the ground state and first excited state is $\phi = 4 \arctan\left(\chi_{qr}/\kappa\right) \approx 40^\circ$.

We calculate the measurement efficiency η at the resonance frequency of the readout resonator by comparing the measured standard deviation $\sigma = 2.0$ $\sqrt{\text{photon}}$ of the ground-state distribution in our histogram with the ideal case, which is $\sigma_{\mathrm{ideal}} = 1/\sqrt{2}$ $\sqrt{\text{photon}}$ for a coherent state [19], and we obtain $\eta = \sigma^2_{\mathrm{ideal}}/\sigma^2 \approx 0.13$.

We can partly attribute the reduction in measurement efficiency to known and expected losses between the readout resonator and the parametric amplifier. Since we use a commercial power combiner to feed in the pump tone, we lower the power incident on the DJJAA by at least a factor of two compared with the calibrated value. Additionally, our sample holder is separated from the amplifier by several microwave components, such as circulators and various connecting cables, which can further add dissipation at the readout frequency. Therefore, a conservative upper bound on the measurement efficiency determined by losses is $\eta_L \leq 0.5$, which, in combination with the measurement efficiency due to the HEMT, implies a conservative bound on the quantum efficiency $\eta_{\mathrm{DJJAA}} = \eta/\eta_L \geq 0.26$ for our parametric amplifier.

An example of a measured quantum-jump trace is depicted in Fig. 5(b) for the same integration time and readout strength as in Fig. 5(a). For the detection of the qubit state, highlighted by the solid red line, we use a multipoint filter [48]. The filter declares a jump when the detected Q value falls into a range of $\pm\sigma$ around the mean values $\bar{Q}_i$ ($i \in g, e, f, h$) associated with the first four qubit states. For the ground and the first excited state, the filter range is color coded by the pink and green areas, respectively, around the mean values, which are indicated by dashed lines. As discussed in Appendix K, from the relative populations of the first four qubit states, we extract a qubit temperature of $T_q = 87$ mK, which is in good agreement with the temperature of the cryostat base plate $T \approx 80$ mK during this experiment. For measurements taken at the base temperature ($T_{\mathrm{base}} = 30$ mK), the qubit temperature saturates at a constant value $T_q \approx 61$ mK.

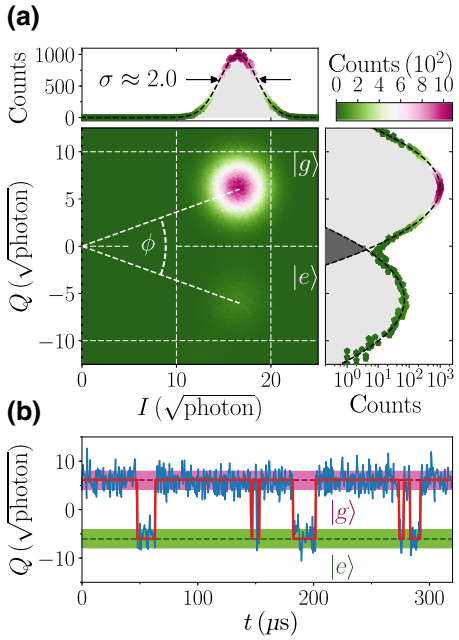

FIG. 5. Quantum-jump measurement. (a) 2D histogram of measured I and Q quadratures of the readout resonator at $f_r = 5.8224$ GHz. The I and Q values are reported in units of the square root of measurement photons $\sqrt{\bar{n}_r \kappa_r T_m/4}$, where $\bar{n}_r \approx 150$, $\kappa_r/2\pi = 2.7$ MHz, and $T_m = 500$ ns, for a total of 6×10^5 counts. We observe two peaks in the I–Q plane, a larger one corresponding to the qubit ground state $|g\rangle$ and a peak approximately ten times smaller corresponding to the first excited state $|e\rangle$. The qubit temperature calculated from the observed populations is $T_q = 87$ mK, in agreement with the base-plate temperature of the dilution refrigerator of 80 mK, which is raised to activate thermal excitations of the qubit. The distribution plots along I (top panel) and Q (right panel) are plotted for slices centered on the ground-state peak. From a Gaussian fit, we extract a standard deviation $\sigma = 2.0$ $\sqrt{\text{photon}}$. (b) Typical example of a measured quantum-jump trace corresponding to the time evolution of the Q quadrature for the same experiment as that shown in (a). The red solid line indicates the qubit state given by a four-point latching filter. The colored areas around the Q values corresponding to $|g\rangle$ (pink) and $|e\rangle$ (green) represent one standard deviation σ, which is the value used for the latching filter.

VII. CONCLUSION

In summary, we demonstrate a type of parametric amplifier based on a dispersion-engineered Josephson-junction array, with up to four hybridized pairs of modes, showing a nondegenerate power gain in excess of 20 dB, within an instantaneous bandwidth in the range of 10 MHz.

The measured noise visibility suggests that our amplifiers approach the quantum limit of added noise. We use the amplifier to measure quantum jumps of a transmon qubit, which we can discriminate with 90% fidelity within 500 ns of integration. For comparison, using state-of-the-art readout-chain optimization and pulse shaping, fidelities of up to 97% can be achieved in 80 ns [63]. The optical fabrication of the JJ array is accessible, reproducible, and low cost.

By optimizing the mode engineering of future amplifiers, it will be possible to build an array with a sufficiently high mode density that a moderate flux tunability will suffice to cover the entire frequency band from 1 GHz up to 10 GHz. Further improvements also include the suppression of unintended higher-order effects by utilizing asymmetric dc SQUIDs [18] or SNAILs [44,45,64].

ACKNOWLEDGMENTS

Funding is provided by the Alexander von Humboldt Foundation in the framework of a Sofja Kovalevskaja Award, endowed by the German Federal Ministry of Education and Research, and by the Initiative and Networking Fund of the Helmholtz Association, within the Helmholtz Future Project "Scalable Solid State Quantum Computing." Furthermore, this research is supported by the ANR under CLOUD contracts (Project No. ANR-16-CE24-0005). PW and WW acknowledge support from a European Research Council MoQuOS advanced grant (Grant No. 741276). IT and AVU acknowledge partial support from the Ministry of Education and Science of the Russian Federation in the framework of the Increased Competitiveness Program of the National University of Science and Technology MISIS (Contract No. K2-2018-015). Use of facilities was supported by the KIT Nanostructure Service Laboratory (NSL). We acknowledge qKit [65] for providing a convenient measurement software framework.

Patrick Winkel and Ivan Takmakov contributed equally.

APPENDIX A: INDUCTANCE AND CAPACITANCE MATRICES

The capacitance and inverse inductance matrices introduced in Eq. (2), $\tilde{C}$ and $\tilde{L}^{-1}$, respectively, are

$$\tilde{C} = \begin{pmatrix} 2C_J + C_0 & -C_J & 0 & \cdots & & & & & & & \\ -C_J & 2C_J + C_0 & -C_J & 0 & \cdots & & & & & & \\ 0 & -C_J & 2C_J + C_0 & -C_J & 0 & \cdots & & & & & \\ \vdots & \ddots & \ddots & \ddots & \ddots & \ddots & \ddots & & & & \\ & & 0 & -C_J & C_J + C_c + C_0' & -C_c & 0 & & & & \\ & & & 0 & -C_c & C_J + C_c + C_0' & -C_J & 0 & & & \\ & & & & 0 & -C_J & 2C_J + C_0 & -C_J & 0 & & \\ & & & & \ddots & \ddots & \ddots & \ddots & \ddots & \vdots & \\ & & & & & \ddots & 0 & -C_J & 2C_J + C_0 & -C_J & \\ & & & & & & \cdots & 0 & -C_J & 2C_J + C_0 & \end{pmatrix} \tag{A1}$$

and

$$\tilde{L}^{-1} = \begin{pmatrix} \frac{2}{L_J} & -\frac{1}{L_J} & 0 & \cdots & & & & & & & \\ -\frac{1}{L_J} & \frac{2}{L_J} & -\frac{1}{L_J} & 0 & \cdots & & & & & & \\ 0 & -\frac{1}{L_J} & \frac{2}{L_J} & -\frac{1}{L_J} & 0 & \cdots & & & & & \\ \vdots & \ddots & \ddots & \ddots & \ddots & \ddots & \ddots & & & & \\ & & 0 & -\frac{1}{L_J} & \frac{1}{L_J} & 0 & 0 & & & & \\ & & & 0 & 0 & \frac{1}{L_J} & -\frac{1}{L_J} & 0 & & & \\ & & & & 0 & -\frac{1}{L_J} & \frac{2}{L_J} & -\frac{1}{L_J} & 0 & & \\ & & & & \ddots & \ddots & \ddots & \ddots & \ddots & \vdots & \\ & & & & & \ddots & 0 & -\frac{1}{L_J} & \frac{2}{L_J} & -\frac{1}{L_J} & \\ & & & & & & \cdots & 0 & -\frac{1}{L_J} & \frac{2}{L_J} & \end{pmatrix}. \tag{A2}$$

The parameters for the SQUID array are the single-SQUID Josephson inductance L_J and junction capacitance C_J, and the capacitance per island to ground C_0. The matrix elements due to the center capacitance C_c and its capacitance to ground C_0' are highlighted in red. Since the array is galvanically connected to its environment at both ends, the boundary conditions are $\Phi_0 = \Phi_{N+1} = 0$. As discussed in the main text, we do not consider long-range Coulomb interactions in the capacitance matrix that could be mediated by the ground plane on the back surface of the sapphire wafer.

APPENDIX B: NONLINEARITY: SELF- AND CROSS-KERR COEFFICIENTS

For JPAs, the nonlinearity arising from the cosine potential of the JJ(s) is an indispensable requirement for the parametric amplification process. However, as discussed in Refs. [37,38], the magnitude of the lowest-order nonlinear terms, referred to as Kerr coefficients, influences the amplifier's saturation power and the required parametric pump power at the same time. Therefore it is important to derive the nonlinearity for the various eigenmodes of our circuit design as a function of the circuit parameters. As described in Ref. [51], we introduce the nonlinearity perturbatively into our linear circuit model. The modal distribution of the eigenmodes enters the two equations for the self- and cross-Kerr coefficients,

$$K_{m,m} = \frac{2\hbar\pi^4 E_J \eta_{mmmm}}{\Phi_0^4 C_J^2 \omega_m^2}, \qquad K_{m,k} = \frac{4\hbar\pi^4 E_J \eta_{mmkk}}{\Phi_0^4 C_J^2 \omega_m \omega_k}, \tag{B1}$$

by means of a dimensionless factor η_{mmkk}:

$$\eta_{mmkk} = \sum_{i=0}^{N} \left\{ \left[\sum_{j=0}^{N} \left(\sqrt{C_J}\tilde{C}_{i,j}^{-1/2} - \sqrt{C_J}\tilde{C}_{i-1,j}^{-1/2} \right) \Psi_{j,m} \right]^2 \times \left[\sum_{j=0}^{N} \left(\sqrt{C_J}\tilde{C}_{i,j}^{-1/2} - \sqrt{C_J}\tilde{C}_{i-1,j}^{-1/2} \right) \Psi_{j,k} \right]^2 \right\}. \tag{B2}$$

Here $\tilde{C}^{-1/2}$ is the square root of the inverse capacitance matrix, defined as $\tilde{C}^{-1/2} \cdot \tilde{C}^{-1/2} = \tilde{C}^{-1}$, and $\Psi_{j,m}$ is the jth entry of the mth eigenvector $\vec{\Psi}_m$ of the eigenvalue problem in Eq. (3).

Generally speaking, the more two eigenmodes overlap in terms of their standing-wave flux distribution along the array, the more strongly they influence each other when driven. Notably, for the antisymmetric modes (with an even mode number n), the jump in the node phase and the node-flux distribution from negative to positive values which occurs at the position of the center capacitance causes unphysical results for the dimensionless factors η_{mmmm} and, as a consequence, artificially large self-Kerr coefficients. Therefore, we calculate the self-Kerr coefficients and the cross-Kerr coefficients for neighboring modes for our devices by symmetrizing these eigenfunctions:

$$\vec{\Psi}_{m,\mathrm{sym}} = \vec{\Psi}_m^T \cdot \tilde{S}. \tag{B3}$$

Here, the diagonal matrix $\tilde{S}$ is

$$\tilde{S} = \mathrm{diag}(1, 1, \ldots, 1, 1, -1, -1, \ldots, -1, -1), \tag{B4}$$

where the change in sign occurs at the entry with index $j = N/2 + 1$. These Kerr coefficients are listed in Table I.

APPENDIX C: CIRCUIT MODEL: DEVICE OVERVIEW

In the main text we discuss three samples, which differ slightly in their design parameters. In Table II, we give an overview of the circuit parameters that enter our model.

We evaluate the overlap areas A_J forming the JJ contact using SEM images. We do not investigate the devices directly, in order to avoid damaging the sample. Instead, we use comparable samples from the same batch in the immediate vicinity of the sample-chip location. The junction capacitance is inferred from the overlap area: $C_J = 50\ \mathrm{fF}/\mu\mathrm{m}^2 \times A_J$. The Josephson inductance per SQUID junction L_J is deduced from room-temperature resistance measurements. The value of the center capacitance is estimated from finite-element simulations. The capacitances to ground of the center capacitor plates are calculated for a standard microstrip geometry with back-surface metallization [66]. Therefore, the only remaining free circuit parameter is the capacitance to ground C_0 of each superconducting island between two SQUID junctions, which we obtain from fitting the dispersion relation (see Fig. 1). The stray inductance L_s of the aluminum leads is estimated from the fits presented in Appendix D. Its contribution to the coupling rate κ to the input port is discussed in Appendix E, and, for simplicity, it is neglected in the linear model used to calculate the dispersion relation (see Fig. 1).

APPENDIX D: FLUX MODULATION AND JOSEPHSON-INDUCTANCE PARTICIPATION RATIO

The modulation of the system eigenmodes ω_n as a function of the bias current I_b applied to the superconducting

TABLE I. Eigenfrequencies ω_m, self-Kerr coefficients $K_{m,m}$, and cross-Kerr coefficients for neighboring modes $K_{m,m+1}$, calculated with our circuit model (see Sec. III) for the first 12 eigenmodes of the three devices discussed in Sec. V. The parameter values for the circuit model are found in Table II for all three devices.

m	$N = 1200$			$N = 1600$			$N = 1800$		
	$\frac{\omega_m}{2\pi}$ (GHz)	$\frac{K_{m,m}}{2\pi}$ (kHz)	$\frac{K_{m,m+1}}{2\pi}$ (kHz)	$\frac{\omega_m}{2\pi}$ (GHz)	$\frac{K_{m,m}}{2\pi}$ (kHz)	$\frac{K_{m,m+1}}{2\pi}$ (kHz)	$\frac{\omega_m}{2\pi}$ (GHz)	$\frac{K_{m,m}}{2\pi}$ (kHz)	$\frac{K_{m,m+1}}{2\pi}$ (kHz)
0	2.061	1.1	2.8	1.113	0.5	1.2	0.863	0.3	0.9
1	2.478	1.8	6.1	1.345	0.8	2.7	1.039	0.6	1.9
2	6.427	12.7	26.9	3.488	5.6	11.9	2.696	3.8	8.2
3	7.106	15.3	29.7	3.927	7.1	13.7	3.050	5.0	9.5
4	10.398	34.9	69.8	5.828	16.4	32.8	4.538	11.5	22.8
5	10.881	37.3	59.6	6.210	18.2	29.4	4.873	12.9	20.9
6	13.364	58.3	115.3	7.819	30.0	58.7	6.177	21.5	41.9
7	13.646	59.8	87.2	8.090	31.4	46.5	6.434	22.8	33.9
8				9.381	43.3	84.7	7.528	32.1	62.4
9				9.560	44.3	62.4	7.710	33.1	46.8
10				10.561	55.0	107.8	8.598	42.0	81.8
11				10.677	55.7	76.1	8.724	42.7	58.5

field coil can be described by an effective lumped-element model for each mode, which consists of a series circuit of a flux-dependent and a flux-independent inductance $L_{J,\mathrm{tot}}(\Phi)$ and L_S, respectively, shunted by a capacitance C. The effective resonance frequency of the lumped-element model can be written as

$$f\ (I_b) = \frac{1}{2\pi\sqrt{C\left[L_S + L_{J,\mathrm{tot}}(I_b)\right]}}. \tag{D1}$$

While $L_{J,\mathrm{tot}}$ originates from the kinetic inductance of the SQUIDs, the effective stray inductance L_s originates from both geometric and kinetic contributions from the superconducting leads connecting the SQUIDs. By fitting the model prediction to the experimentally observed frequency modulation, we can calculate the Josephson-inductance participation ratio $\gamma_L = L_{J,\mathrm{tot}}/\left(L_{J,\mathrm{tot}} + L_S\right)$, and also calibrate the effective bias flux $\Phi = \Phi_b + \Phi_{\mathrm{offset}}$ in units of Φ_0. The bias flux Φ_b is due to the current I_b applied to the coil, and Φ_{offset} is a static offset.

TABLE II. Overview of the circuit parameters of the devices: number of SQUID junctions N, room-temperature resistance of the array from the input port to the center capacitance $R_{n,\mathrm{in}}$, room-temperature resistance of the array from the center capacitance to ground $R_{n,\mathrm{out}}$, resistance asymmetry between the two array sections m, room-temperature resistance of a single SQUID junction $R_{n,\mathrm{SQ}}$, critical current of a single SQUID junction $I_{c,\mathrm{SQ}}$, Josephson inductance of a single SQUID junction L_J, stray inductance L_s, kinetic-inductance participation ratios $\gamma_{L,\mathrm{fit}}$ (see Appendix D) and $\gamma_L = L_J/(L_J + L_s)$, junction area A_J, junction capacitance C_J, center capacitance C_c, capacitance to ground C_0' (for center capacitance), capacitance to ground per island C_0, and plasma frequency ω_{pl}.

	Sample I	Sample II	Sample III
N	1200	1600	1800
$R_{n,\mathrm{in}}$ (kΩ)	29.03	70.96	102.25
$R_{n,\mathrm{out}}$ (kΩ)	28.41	71.3	102.91
m	1.022	0.995	0.994
$R_{n,\mathrm{SQ}}$ (Ω)	41.5	82.5	108
I_c (μA)	6.0	3.0	2.3
L_J (pH)	55	110	143
L_s (pH)	12.6	12.6	13.3
$\gamma_{L,\mathrm{fit}}$	0.67	0.87	0.92 ± 2
γ_L	0.81	0.90	0.91
A_J (μm^2)	10.8 ± 0.4	10.5 ± 0.4	10.5 ± 0.4
C_J (fF)	1080 ± 40	1050 ± 40	1050 ± 40
C_c (fF)	30	40	45
C_0' (fF)	33	33	33
C_0 (fF)	0.39	0.40	0.42
$\omega_{\mathrm{pl}}/2\pi$ (GHz)	20.65	14.81	13.0

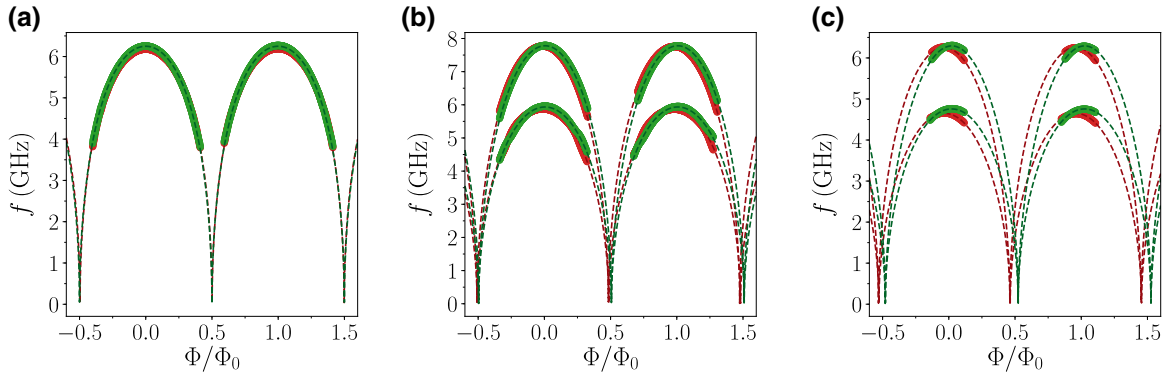

FIG. 6. Fitted uncoupled eigenfrequencies (i.e., $J = 0$) of the three devices discussed in the main text, (a) $N = 1200$, dimer number $n = 2$, (b) $N = 1600$, $n \in \{3, 4\}$, (c) $N = 1800$, $n \in \{3, 4\}$, as a function of the effective external flux Φ. The data points are extracted from the measurement data depicted in Fig. 2 by fitting Eq. (G1) to the frequency dependence of the reflection coefficient and following the calculation described in Appendix G. The color-coded dashed lines are the fit results according to Eq. (D5), from which we extract the Josephson-inductance participation ratio γ_L. In the absence of field offsets and asymmetries in the array, the red and green curves should overlap perfectly. While the first device operates in a rather uniform magnetic environment, the latter two see an external stray-magnetic-field gradient. However, the stray-field gradient has an influence on the hybridization only for the last sample, since the coupling between neighboring modes J_n is weaker.

The current dependence of $L_{J,\mathrm{tot}}$ is deduced from the flux-dependent inductance of a single symmetric dc SQUID, which is given by

$$L_{J,\mathrm{tot}}(\Phi) = \frac{L_{J,\mathrm{tot}}(0)}{|\cos(\pi\Phi/\Phi_0)|}. \tag{D2}$$

Assuming a linear dependence between the external bias flux created by the superconducting coil and the bias current, Eq. (D2) can be expressed as a function of the bias current as follows:

$$L_{J,\mathrm{tot}}(I_b) = \frac{L_{J,\mathrm{tot}}(0)}{|\cos[\pi l_b(I_b + I_{\mathrm{offset}})]|}. \tag{D3}$$

The parameter l_b translates the applied current bias into an external flux bias expressed in terms of the number of magnetic flux quanta. The parameter I_{offset} accounts for the presence of an offset flux due to stray magnetic fields produced by the attached circulator and other components of the setup, or the Earth's magnetic field.

By inserting Eq. (D3) into Eq. (D1), we can write the fit function for the current modulation of the resonance frequencies as

$$f(I_b) = \frac{1}{2\pi\sqrt{C\left\{L_S + L_{J,\mathrm{tot}}(0)/|\cos[\pi l_b(I_b + I_{\mathrm{offset}})]|\right\}}}. \tag{D4}$$

By inserting the Josephson-inductance participation ratio $\gamma_L = L_{J,\mathrm{tot}}(0)/\left[L_S + L_{J,\mathrm{tot}}(0)\right]$ into Eq. (D4) and introducing the frequency amplitude $f_0 = 1/\{2\pi\sqrt{C[L_S + L_{J,\mathrm{tot}}(0)]}\}$, we obtain the final expression for the fitting function used in Figs. 2 and 6:

$$f(I_b) = \frac{f_0}{\sqrt{1 + \gamma_L\left\{1 + |\cos[\pi l_b(I_b + I_{\mathrm{offset}})]|^{-1}\right\}}}. \tag{D5}$$

For each array, we extract a Josephson-inductance participation ratio γ_L between 0.67 and 0.92, as listed in Table II. These values are consistent with estimates based on the geometry and the thickness of the aluminum film, for which we expect a stray kinetic sheet inductance of 1.3 pH/□ and a stray geometric inductance [66] of 1.5 pH/μm, amounting to a total stray inductance per SQUID of 15 ± 4 pH.

APPENDIX E: COUPLING TO THE ENVIRONMENT

The coupling strength κ of the amplifier modes to the input port, which is implemented with a transmission line of characteristic impedance $Z_0 = 50\ \Omega$, is calculated by a transmission-matrix approach [67]. In this formalism, the total transmission matrix $\tilde{T}$ of the amplifier is calculated by multiplying the individual transmission matrices $\tilde{T}_i$ associated with each circuit element, e.g., the SQUIDs, superconducting islands, and stray inductances:

$$\tilde{T} = \prod_{i=1}^{N+1} \tilde{T}_i = \begin{pmatrix} A & B \\ C & D \end{pmatrix}. \tag{E1}$$

Here, N is the total number of SQUIDs. Notably, the sum runs over $N + 1$ entries due to the additional site introduced by the center capacitance C_c. The individual circuit

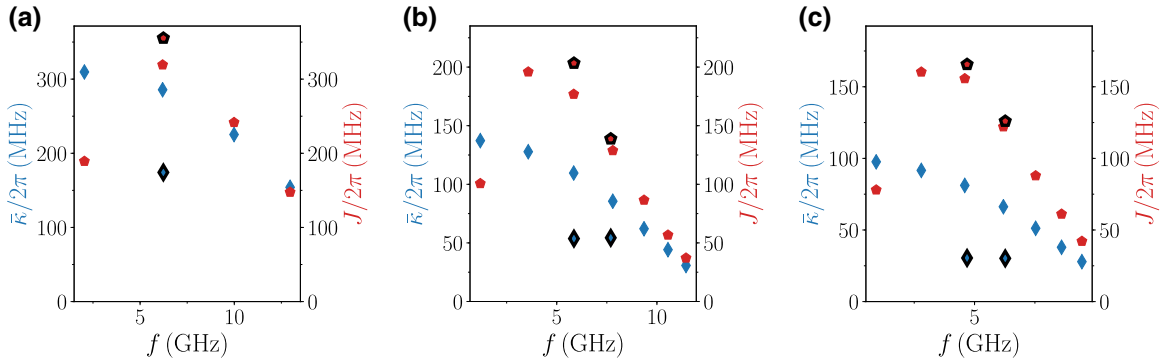

FIG. 7. Calculated external coupling rate κ (blue diamonds) and dimer mode splitting J (red pentagons) as a function of the mode frequency predicted by our transmission-matrix model. The corresponding circuit parameters used for the calculation are listed in Table II. The experimental data are depicted by symbols with an additional black frame and are extracted at the sweet spot of the flux for each mode by fitting Eq. (G1) to the measured complex reflection coefficient in the close vicinity. The results presented in panels (a)–(c) correspond to the samples discussed in the main text (see Fig. 2), with $N = 1200$, $N = 1600$, and $N = 1800$, respectively.

elements expressed as transmission matrices are

$$\begin{aligned}
\tilde{T}_{\mathrm{LS}} &= \begin{pmatrix} 1 & j\omega L_{\mathrm{stray}} \\ 0 & 1 \end{pmatrix}, \\
\tilde{T}_{\mathrm{SQ}} &= \begin{pmatrix} 1 & \left[(j\omega L_J)^{-1} + j\omega C_J\right]^{-1} \\ 0 & 1 \end{pmatrix}, \\
\tilde{T}_{C_0} &= \begin{pmatrix} 1 & 0 \\ j\omega C_0 & 1 \end{pmatrix}, \\
\tilde{T}_{C_c} &= \begin{pmatrix} 1 & 1/j\omega C_c \\ 0 & 1 \end{pmatrix}, \\
\tilde{T}_{C_0'} &= \begin{pmatrix} 1 & 0 \\ j\omega C_0' & 1 \end{pmatrix}.
\end{aligned} \tag{E2}$$

Here, j is the imaginary unit according to electrical-engineering standards ($j = -i$), L_{stray} is the stray inductance due to the pure aluminum islands, L_J and C_J are the Josephson inductance and capacitance, respectively, for each SQUID junction, C_0 is the capacitance of an island to ground, C_c is the center capacitance, and C_0' is the capacitance of the capacitor plates to ground. The total transmission matrix of our amplifiers is composed of a repetition of three elements ($\tilde{T}_{\mathrm{LS}}$, $\tilde{T}_{\mathrm{SQ}}$ and $\tilde{T}_{c_0}$) N times, with the contribution of the center capacitance ($\tilde{T}_{C_0'}$ and $\tilde{T}_{C_c}$) in the middle:

$$\tilde{T} = \left(\prod_{i=1}^{N/2} \tilde{T}_{\mathrm{LS}}\tilde{T}_{\mathrm{SQ}}\tilde{T}_{c_0}\right) \tilde{T}_{C_0'}\tilde{T}_{C_c}\tilde{T}_{C_0'} \left(\prod_{i=1}^{N/2} \tilde{T}_{\mathrm{LS}}\tilde{T}_{\mathrm{SQ}}\tilde{T}_{c_0}\right). \tag{E3}$$

From the total transmission matrix $\tilde{T}$, the complex reflection coefficient S_{11} is calculated:

$$S_{11} = \frac{A + B/Z_0 - CZ_0 - D}{A + B/Z_0 + CZ_0 + D}. \tag{E4}$$

For the input port, we assume a characteristic impedance $Z_0 = 50\ \Omega$. By solving Eq. (E4) in the frequency range up to the plasma frequency $\omega \in [0, \omega_{\mathrm{pl}}]$ numerically, we can extract the eigenfrequencies, the external coupling rate κ_n, and the level splitting J_n for each dimer individually. Figure 7 depicts the numerical calculation and the extracted experimental data (shown by markers with black frames) for the three samples discussed in the main text. As also stated in the main text, the coupling rate J_n shows a domelike structure, while the coupling rate continuously decreases.

APPENDIX F: SAMPLE HOLDER

The amplifiers, with physical dimensions of $7.5 \times 3.6\ \mathrm{mm}^2$, are glued onto a copper sample holder with silver paste. For the external connection to the on-chip input port, we use a printed circuit board (PCB) with a 50-Ω microstrip transmission line [see Fig. 8(a)]. The PCB is covered with copper on both sides, enclosing a low-loss dielectric ($\epsilon_r = 9.9$) of thickness $t = 635\ \mu$m. The height difference between the PCB and the sapphire wafer ($t = 330\ \mu$m) is compensated by a small copper post (not visible) below the sample. The PCB transmission line is directly soldered to the center conductor of an SMA connector. The other half of the PCB's top plate remains covered with copper and serves as a ground for our amplifiers. For that reason, we use vias to galvanically connect the top copper plate to the sample holder. The amplifier is connected to the PCB at both ends with aluminum wire bonds. Each amplifier is equipped with a superconducting bias coil integrated into the lid of the sample holder, and with a commercial circulator directly mounted on the SMA input port to avoid low-frequency standing waves [see Fig. 8(b)].

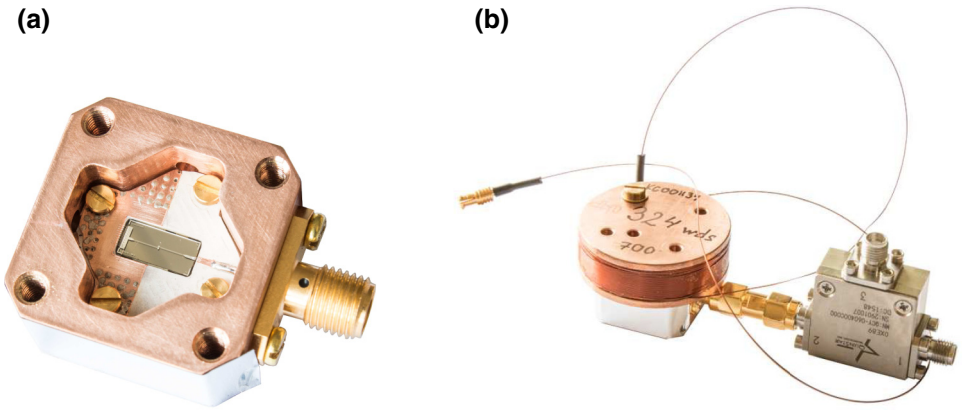

FIG. 8. (a) Body of the copper sample holder (without lid), hosting a printed circuit board, with a 7.5×3.6 mm^2 sapphire wafer in the center. The PCB is glued with silver paste and attached with four brass screws. (b) Closed copper sample holder, with a superconducting bias coil integrated into its lid, and a commercial circulator directly mounted on the SMA connector.

APPENDIX G: LINEAR CHARACTERIZATION OF DIMERS

In our devices, the frequency detuning between neighboring dimers $\Delta\omega$ is much larger than the frequency detuning $2J_n$ between a pair of modes that form a dimer. Therefore, we can neglect the other modes of the array when measuring a device in the close vicinity of a dimer. In this limit, and assuming a weak probe tone, the measured reflection coefficient Γ is simply the product of two modes with resonance frequencies ω_+ and ω_-, external coupling rates κ_+ and $\kappa-$ to the input port, and internal loss rates γ_+ and γ_-. In the ideal case, without any variations along the array in terms of the critical current and external offset flux, the two external coupling rates are identical ($\kappa_+ = \kappa_-$). The reflection coefficient of the dimer is

$$\Gamma = \prod_{m\in\{+,-\}} \Gamma_m e^{i\phi_0}, \tag{G1}$$

where ϕ_0 is an arbitrary offset phase determined by the measurement setup, and Γ_m is the standard reflection coefficient of a linear single-port resonator,

$$\Gamma_m = -1 + \frac{\kappa_m(\kappa_m+\gamma_m)/2 + i\kappa_m(\omega-\omega_i)}{(\omega-\omega_0)^2 + (\kappa_m+\gamma_m)^2/4}. \tag{G2}$$

In the case where the external coupling rates $\kappa_\pm$ are not identical, we can gain information about the variation, mainly in terms of the Josephson energy, along the array by performing a basis transformation. Instead of describing the system by its eigenmodes, which are determined by Eq. (2), we can treat each dimer as a system of two oscillators with resonance frequencies ω_1 and ω_2 that are linearly coupled with rate J_n, similarly to Ref. [18]:

$$H = \hbar\omega_1 \mathbf{a}_1^\dagger \mathbf{a}_1 + \hbar\omega_2 \mathbf{a}_2^\dagger \mathbf{a}_2 + J_n\left(\mathbf{a}_1^\dagger \mathbf{a}_2 + \mathbf{a}_1 \mathbf{a}_2^\dagger\right). \tag{G3}$$

In this picture, the two oscillators correspond to the parts of the array before and after the center capacitor, as seen from the input port. The measured eigenfrequencies ω_+ and ω_- expressed in this new basis are

$$\omega_\pm = \frac{\omega_1+\omega_2}{2} \pm \sqrt{\left(\frac{\omega_1-\omega_2}{2}\right)^2 + J_n^2}. \tag{G4}$$

Since only the first part of the array is coupled to the input port with rate κ, a variation in the circuit parameters along the array ($\omega_1 \neq \omega_2$) will induce two different external coupling rates

$$\kappa_\pm = \frac{\kappa}{2}\left(1 \pm \frac{\omega_1-\omega_2}{\sqrt{4J_n^2 + (\omega_1-\omega_2)^2}}\right), \tag{G5}$$

with $\kappa = \kappa_+ + \kappa_-$. By inserting Eq. (G4) into Eq. (G5), we derive an expression for the frequency asymmetry A along the array that depends only on the experimentally accessible quantities $\omega_\pm$ and $\kappa_\pm$:

$$A = (\omega_1-\omega_2)^2 = \frac{(\kappa_+-\kappa_-)^2(\omega_+-\omega_-)^2}{(\kappa_++\kappa_-)^2}. \tag{G6}$$

Finally, the bare frequencies ω_1 and ω_2 in the new basis are

$$\omega_{1,2} = \frac{\omega_++\omega_-}{2} \pm \frac{A}{2}. \tag{G7}$$

APPENDIX H: FLUX TUNABILITY

For a DJJAA device with $N = 1300$ SQUIDs, we investigate the flux tunability by measuring the power gain under different external-bias-flux conditions. Figure 9(a) depicts the phase response of the amplifier, similarly to Fig. 2, where the main features are the second ($n = 2$), third ($n = 3$), and fourth ($n = 4$) dimers of the device. By changing the bias flux and adjusting the pump parameters (frequency and power), we observe a signal power gain reaching 20 dB in a frequency range $\delta f \geq 1.5$ GHz [see Fig. 9(b)] spanning between the highest and lowest lobes of the dimer for all three dimers.

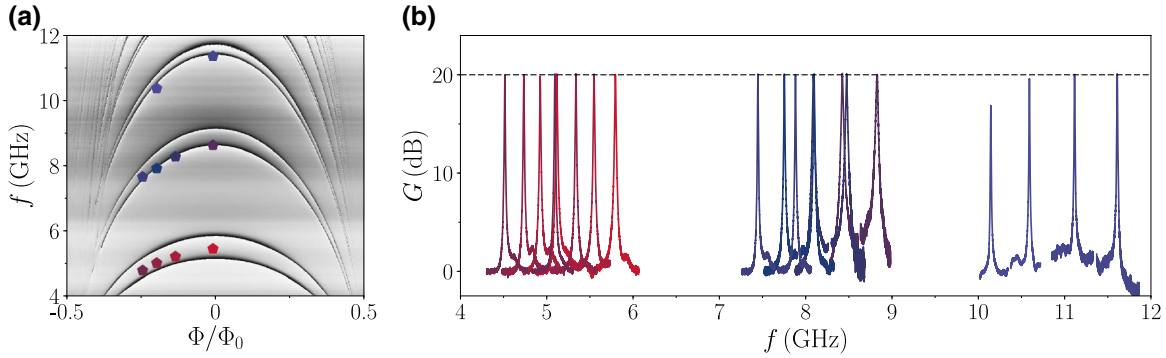

FIG. 9. (a) Phase of the complex reflection coefficient $\arg(S_{11})$ in radians as a function of probe frequency f and external bias flux Φ, normalized to the flux quantum Φ_0, for a DJJAA with $N = 1300$ SQUIDs. The grayscale covers the range from $-\pi$ (black) to π (white). The main features in the given frequency range are the second ($n = 2$), third ($n = 3$), and fourth ($n = 4$) dimers of the device, with higher-frequency eigenmodes becoming visible close to full SQUID frustration ($\Phi/\Phi_0 = 0.5$). The pentagons highlight the bias flux and pump frequency used to measure the power gain close to the dimer modes. (b) Power gain G in dB as a function of probe frequency f for bias fluxes and pump frequencies color-coded according to the pentagons in (a). The tunable bandwidth of this device, measured from the lowest frequency to the highest frequency of each dimer at which we reach $G = 20$ dB, exceeds 1.5 GHz for all three dimers. This is a typical value for our devices.

APPENDIX I: QUBIT CHARACTERIZATION

For the coupled qubit-resonator system, the full Hamiltonian can be written as

$$\hat{H} = 4E_{c,q}\hat{N}^2 - E_{J,q}\cos(\hat{\Theta}) + \hbar\omega_r\hat{a}^\dagger\hat{a} + \hbar g\hat{N}\left(\hat{a} + \hat{a}^\dagger\right), \tag{I1}$$

where $\hat{N}$ is the number operator of the Cooper pairs transferred over the Josephson junction, $\hat{\Theta}$ is the superconducting phase difference across the JJ, $E_{c,q}$ is the charging energy due to its shunt capacitance, and $E_{J,q}$ is the Josephson energy. Furthermore, $\hat{a}^\dagger$ and $\hat{a}$ are the creation and annihilation operators of the bare cavity mode with angular frequency ω_r. The electric field of the resonator $\hat{E} \propto (\hat{a}^\dagger + \hat{a})$ couples to the qubit's electric dipole moment with a coupling rate g.

For a ratio $E_{J,q}/E_{c,q} \geq 50$, usually referred to as the transmon regime, the qubit itself is described by a nonlinear resonator with a bare resonance frequency ω_q and a relatively small anharmonicity $\alpha_q \ll \omega_q$. In the dispersive limit, the qubit is weakly coupled to the resonator, i.e., $g \ll \Delta = |\omega_r - \omega_q|$, and imposes only a small frequency shift χ_{qr} on the resonator according to its state. Hence, for small probe powers and weak coupling, the system Hamiltonian given in Eq. (I1) is simplified by considering a reduced Hilbert space only [9,68]:

$$\frac{\hat{H}_{\text{low}}}{\hbar} = \tilde{\omega}_q\hat{a}_q^\dagger\hat{a}_q - \frac{\alpha_q}{2}\left(\hat{a}_q^\dagger\right)^2\hat{a}_q^2 - \chi_{qr}\hat{a}_q^\dagger\hat{a}_q\hat{a}_r^\dagger\hat{a}_r + \tilde{\omega}_r\hat{a}_r^\dagger\hat{a}_r - \frac{\alpha_r}{2}\left(\hat{a}_r^\dagger\right)^2\hat{a}_r^2, \tag{I2}$$

where $\hat{a}_i^\dagger$ and $\hat{a}_i$ with $i = (q, r)$ are the creation and annihilation operators of the dressed fundamental qubit and readout-resonator modes, with angular frequencies $\tilde{\omega}_q$ and $\tilde{\omega}_r$ and self-Kerr coefficients α_q and α_r, respectively. The cross-Kerr coefficient between the two modes, denoted by χ_{qr}, determines the dispersive shift of the resonator induced by the qubit state and the dependence of the qubit's first transition frequency $\tilde{\omega}_q$ on the mean number of photons circulating in the resonator $\bar{n}_r$:

$$\tilde{\omega}_q(\bar{n}) = \tilde{\omega}_q^0 - \chi_{qr}\bar{n}_r. \tag{I3}$$

From a circle fit to the complex response of the readout resonator [see Fig. 10(a)], we extract the resonator frequency $\tilde{\omega}_r/2\pi = 5.8224$ GHz and the total linewidth $\kappa_r/2\pi \approx 2.7$ MHz. By applying a second tone at a frequency f_{drive} to the qubit while continuously monitoring the reflected phase of the readout resonator at resonance, we measure the qubit spectrum [see Fig. 10(b)]. The first transition frequency $f_{\text{ge}} = \tilde{\omega}_q/2\pi$ is found at $f_{\text{drive}} = 4.505$ GHz, with an anharmonicity $\alpha_q/2\pi = 256$ MHz compared with the next higher transition f_{ef}. For higher drive powers P_{drive}, several multiphoton transitions appear. The dispersive shift is found to be $\chi_{qr}/2\pi = 480$ kHz from a histogram of the I-Q plane, by separating the ground state and first excited state of the qubit with the aid of our DJJAA (see Fig. 5).

In order to extract the circuit parameters $E_{J,q}$, $E_{c,q}$, g, and ω_r of the system Hamiltonian given in Eq. (I1), we numerically solve for the lowest eigenenergies in the charge basis for the qubit and in the Fock basis for the readout resonator $|N, n\rangle$ [9]. We compare the results with the experimentally observed values measured at low readout powers, where the system is approximated by the Hamiltonian in Eq. (I2). We find $E_{J,q}/h = 12.5$ GHz, $E_{c,q}/h = 225$ MHz $\left(E_{J,q}/E_{c,q} \approx 56\right)$, and $g = 39$ MHz, which are in good agreement with values extracted from

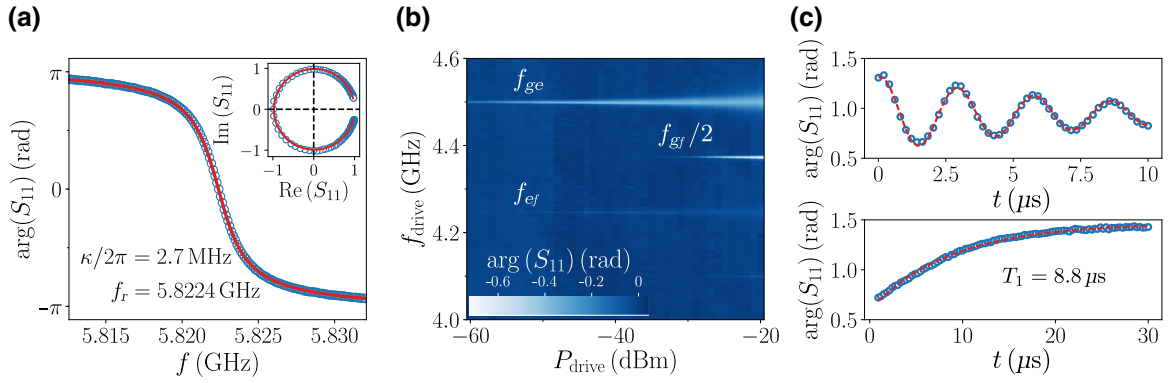

FIG. 10. Characterization of transmon qubit. (a) Phase of the complex reflection coefficient $\arg(S_{11})$ as a function of probe frequency f for the readout resonator highlighted in Fig. 3. The resonance frequency $f_r = 5.8224$ GHz and total linewidth $\kappa/2\pi = 2.7$ MHz are extracted from a circle fit, which is indicated by the solid red line. As shown in the inset, the radius of the resonator response in the complex plane is approximately 1, implying $Q_i \gg Q_c$. (b) Qubit spectrum measured by monitoring the resonator's phase response at resonance in a two-tone spectroscopy experiment. The first transition frequency appears at $f_{ge} \approx 4.505$ GHz, while the second transition frequency is $f_{ef} \approx 4.244$ GHz, resulting in an anharmonicity $\alpha_q \approx 256$ MHz. Additionally, several multiphoton transitions are visible. (c) Rabi oscillations of the qubit (top panel) and energy-relaxation measurement (bottom panel) following a π-pulse. The π-pulse duration of 1.5 μs corresponds to the first minimum of the measured Rabi oscillations. We extract an energy relaxation time of $T_1 = 8.8$ μs. From a Ramsey-fringe measurement [62] (see Fig. 11), we extract a coherence time $T_2^\star = 6.5$ μs.

finite-element simulations for the charging energy and from room-temperature resistance measurements for the Josephson energy.

By applying a drive tone to the qubit at its fundamental transition frequency $\tilde{f}_q$ with a rectangular envelope of varying duration t, we observe continuous Rabi oscillations between the qubit's ground and first excited state [see top panel in Fig. 10(c)]. Using a relatively weak drive strength, we calibrate the duration of a π-pulse as $t_\pi \approx 1.43$ μs by fitting the data (blue) with a periodic cosine function with an exponentially decaying envelope (red). By exciting the qubit to its first excited state and gradually increasing the time interval t between the end of the excitation pulse and the beginning of the readout pulse, we perform an energy-relaxation measurement. From an exponential fit (red) to the data (blue), the corresponding energy relaxation time is found to be $T_1 \approx 8.8$ μs [see bottom panel in Fig. 10(c)]. The qubit's coherence time, extracted from a Ramsey-fringe measurement, is $T_2^\star \approx 6.5$ μs (see Fig. 11).

APPENDIX J: PHOTON-NUMBER CALIBRATION

Figure 11(a) depicts the calibrated photon number as a function of the input power. As expected, the photon number increases linearly with the drive power, i.e., $P_{\mathrm{drive}} \propto \bar{V}^2_{\mathrm{drive}}$. The changes in the Ramsey frequency f_R and the observed coherence time $T_2^\star$ are illustrated in Fig. 11(b) for two different drive strengths. Notably, the decrease in coherence results from an increasing distribution of the coherent state in the Fock basis, which is proportional to $\bar{V}_{\mathrm{drive}}$ [69]. We fit the measured oscillations with an exponentially damped cosine

$$\varphi(\tau) = e^{-\tau/T_2^\star} A \cos\left[2\pi(f_R\tau) + \phi_0\right] + \varphi_0. \tag{J1}$$

Here τ is the evolution time during the experiment, $T_2^\star$ is the coherence time, A is the oscillation amplitude, f_R is the Ramsey frequency, ϕ_0 is the offset phase of the cosine oscillation, and φ_0 is the global offset phase. In the case of two distinct Ramsey frequencies, as depicted in Fig. 11, we use an extended fit function $\varphi(\tau)$:

$$\begin{aligned}\varphi(\tau) = \exp^{-\tau/T_2^\star}(&A_1\cos[2\pi(f_{R,1}\tau) + \phi_{0,1}] \\ &+ A_2\cos[2\pi(f_{R,2}\tau) + \phi_{0,2}]) + \varphi_0.\end{aligned} \tag{J2}$$

Most probably, the two distinct Ramsey frequencies $f_{R,1}$ and $f_{R,2}$ arise from two distinct qubit frequencies. However, the origin of these two distinct qubit frequencies remains unknown.

APPENDIX K: QUBIT TEMPERATURE

The effective temperature T_q of a qubit (see Fig. 5) is calculated from the relative occupation of the qubit states with eigenenergy E_k. For a superconducting charge qubit in the transmon regime ($E_{J,q}/E_{c,q} \geq 50$), the eigenenergies are approximately given by Ref. [47]:

$$E_k \approx -E_{J,q} + \sqrt{8E_{J,q}E_{c,q}}\left(k + \frac{1}{2}\right) - \frac{E_{c,q}}{12}(6k^2 + 6k + 3). \tag{K1}$$

The deviations from numerical solutions of the exact charge-qubit Hamiltonian, given in Eq. (I1), are found to

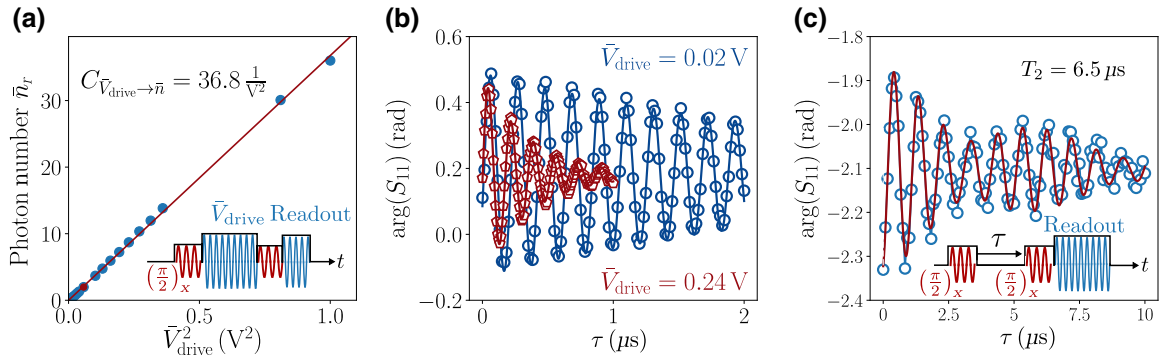

FIG. 11. (a) Photon-number calibration of the readout strength $\bar{V}^2_{\rm drive}$. The pulse sequence used in the experiment is depicted in the lower right corner. Between two $(\pi/2)_x$ pulses applied to the qubit, we apply an additional tone to the readout resonator with a varying voltage amplitude $\bar{V}_{\rm drive}$, before we read out the resonator (qubit state). From the change in frequency f_R observed in the Ramsey fringes [see panel (b)] with respect to the undriven case $f_R^{\,0} = |f_{q,\rm drive} - f_q|$, and using the dispersive shift χ_{qr} (see Fig. 5), we calibrate the photon number $\bar{n}_r$ as a function of the applied drive power $P_{\rm drive} \propto \bar{V}^2_{\rm drive}$. (b) Two examples of measured Ramsey fringes, with $\bar{V}_{\rm drive} = 0.02$ V (blue) and $\bar{V}_{\rm drive} = 0.24$ V (red). Besides the change in the frequency f_R, the measured coherence time $T_2^\star$ decreases also due to measurement-induced dephasing. (c) Standard Ramsey-fringe experiment without an additional drive applied to the readout resonator. Notice the longer time scale compared with panel (b); the pulse sequence is depicted in the lower right-hand corner. We observe two oscillations with similar frequencies $f_R^{\,1} = 1.03$ MHz and $f_R^{\,2} = 1.19$ MHz, with a characteristic decay time $T_2^\star = 6.5\ \mu$s which we extract from a fit to the data according to Eq. J2 (red solid line).

be negligible for qubit states inside the Josephson potential. For a thermal state, the occupation N_k of the kth energy state follows a Boltzmann distribution

$$N_k \propto e^{-(E_k/k_B T_q)}, \tag{K2}$$

where k_B is the Boltzmann constant. Under this assumption, we calculate the effective qubit temperature from the Boltzmann factor of the first two eigenstates as

$$T_q = \frac{E_1 - E_0}{k_B \ln(N_0/N_1)} \tag{K3}$$

if we cannot distinguish more than two qubit states, or by fitting a Boltzmann distribution to the relative occupation

$$N_k(\epsilon')/N = n_0 e^{-(\epsilon_k/k_B T_q)}, \tag{K4}$$

with the parameter $\epsilon_k = (E_k - E_0)$.

[1] F. Mallet, F. R. Ong, A. Palacios-Laloy, F. Nguyen, P. Bertet, D. Vion, and D. Esteve, Single-shot qubit readout in circuit quantum electrodynamics, Nat. Phys. **5**, 791 (2009).

[2] B. Abdo, F. Schackert, M. Hatridge, C. Rigetti, and M. Devoret, Josephson amplifier for qubit readout, Appl. Phys. Lett. **99**, 162506 (2011).

[3] R. Vijay, D. H. Slichter, and I. Siddiqi, Observation of Quantum Jumps in a Superconducting Artificial Atom, Phys. Rev. Lett. **106**, 110502 (2011).

[4] D. Ristè, J. G. van Leeuwen, H.-S. Ku, K. W. Lehnert, and L. DiCarlo, Initialization by Measurement of a Superconducting Quantum Bit Circuit, Phys. Rev. Lett. **109**, 050507 (2012).

[5] Z. R. Lin, K. Inomata, W. D. Oliver, K. Koshino, Y. Nakamura, J. S. Tsai, and T. Yamamoto, Single-shot readout of a superconducting flux qubit with a flux-driven Josephson parametric amplifier, Appl. Phys. Lett. **103**, 132602 (2013).

[6] T. Walter, P. Kurpiers, S. Gasparinetti, P. Magnard, A. Potočnik, Y. Salathé, M. Pechal, M. Mondal, M. Oppliger, C. Eichler, and A. Wallraff, Rapid High-Fidelity Single-Shot Dispersive Readout of Superconducting Qubits, Phys. Rev. Appl. **7**, 054020 (2017).

[7] A. Wallraff, D. I. Schuster, A. Blais, L. Frunzio, R.-S. Huang, J. Majer, S. Kumar, S. M. Girvin, and R. J. Schoelkopf, Strong coupling of a single photon to a superconducting qubit using circuit quantum electrodynamics, Nature **431**, 162 (2004).

[8] A. Blais, R.-S. Huang, A. Wallraff, S. M. Girvin, and R. J. Schoelkopf, Cavity quantum electrodynamics for superconducting electrical circuits: An architecture for quantum computation, Phys. Rev. A **69**, 062320 (2004).

[9] R. Lescanne, L. Verney, Q. Ficheux, M. H. Devoret, B. Huard, M. Mirrahimi, and Z. Leghtas, Escape of a Driven Quantum Josephson Circuit Into Unconfined States, Phys. Rev. Appl. **11**, 014030 (2019).

[10] L. Verney, R. Lescanne, M. H. Devoret, Z. Leghtas, and M. Mirrahimi, Structural Instability of Driven Josephson Circuits Prevented by an Inductive Shunt, Phys. Rev. Appl. **11**, 024003 (2019).

[11] B. Yurke and E. Buks, Performance of cavity-parametric amplifiers, employing kerr nonlinearites, in the presence of two-photon loss, J. Lightwave Technol. **24**, 5054 (2006).

[12] M. A. Castellanos-Beltran and K. W. Lehnert, Widely tunable parametric amplifier based on a superconducting quantum interference device array resonator, Appl. Phys. Lett. **91**, 083509 (2007).

[13] T. Yamamoto, K. Inomata, M. Watanabe, K. Matsuba, T. Miyazaki, W. D. Oliver, Y. Nakamura, and J. S. Tsai,

Flux-driven Josephson parametric amplifier, Appl. Phys. Lett. **93**, 042510 (2008).

[14] N. Bergeal, F. Schackert, M. Metcalfe, R. Vijay, V. E. Manucharyan, L. Frunzio, D. E. Prober, R. J. Schoelkopf, S. M. Girvin, and M. H. Devoret, Phase-preserving amplification near the quantum limit with a Josephson ring modulator, Nature **465**, 64 (2010).

[15] M. Hatridge, R. Vijay, D. H. Slichter, J. Clarke, and I. Siddiqi, Dispersive magnetometry with a quantum limited squid parametric amplifier, Phys. Rev. B **83**, 134501 (2011).

[16] N. Roch, E. Flurin, F. Nguyen, P. Morfin, P. Campagne-Ibarcq, M. H. Devoret, and B. Huard, Widely Tunable, Nondegenerate Three-Wave Mixing Microwave Device Operating Near the Quantum Limit, Phys. Rev. Lett. **108**, 147701 (2012).

[17] J. Y. Mutus *et al.*, Design and characterization of a lumped element single-ended superconducting microwave parametric amplifier with on-chip flux bias line, Appl. Phys. Lett. **103**, 122602 (2013).

[18] C. Eichler, Y. Salathe, J. Mlynek, S. Schmidt, and A. Wallraff, Quantum-Limited Amplification and Entanglement in Coupled Nonlinear Resonators, Phys. Rev. Lett. **113**, 110502 (2014).

[19] C. M. Caves, Quantum limits on noise in linear amplifiers, Phys. Rev. D **26**, 1817 (1982).

[20] P. A. Franken, A. E. Hill, C. W. Peters, and G. Weinreich, Generation of Optical Harmonics, Phys. Rev. Lett. **7**, 118 (1961).

[21] A. A. Clerk, M. H. Devoret, S. M. Girvin, F. Marquardt, and R. J. Schoelkopf, Introduction to quantum noise, measurement, and amplification, Rev. Mod. Phys. **82**, 1155 (2010).

[22] B. Josephson, Possible new effects in superconductive tunnelling, Phys. Lett. **1**, 251 (1962).

[23] K. Likharev, *Dynamics of Josephson Junctions and Circuits* (Gordon and Breach, New York, 1986).

[24] B. Yurke, L. R. Corruccini, P. G. Kaminsky, L. W. Rupp, A. D. Smith, A. H. Silver, R. W. Simon, and E. A. Whittaker, Observation of parametric amplification and deamplification in a Josephson parametric amplifier, Phys. Rev. A **39**, 2519 (1989).

[25] C. C. Chin, D. E. Oates, G. Dresselhaus, and M. S. Dresselhaus, Nonlinear electrodynamics of superconducting NbN and Nb thin films at microwave frequencies, Phys. Rev. B **45**, 4788 (1992).

[26] E. A. Tholén, A. Ergül, K. Stannigel, C. Hutter, and D. B. Haviland, Parametric amplification with weak-link nonlinearity in superconducting microresonators, Phys. Scr. **T137**, 014019 (2009).

[27] N. Maleeva, L. Grünhaupt, T. Klein, F. Levy-Bertrand, O. Dupre, M. Calvo, F. Valenti, P. Winkel, F. Friedrich, W. Wernsdorfer, A. V. Ustinov, H. Rotzinger, A. Monfardini, M. V. Fistul, and I. M. Pop, Circuit quantum electrodynamics of granular aluminum resonators, Nat. Commun. **9**, 3889 (2018).

[28] A. Roy and M. Devoret, Introduction to parametric amplification of quantum signals with Josephson circuits, C.R. Phys. **17**, 740 (2016).

[29] B. H. Eom, P. K. Day, H. G. LeDuc, and J. Zmuidzinas, A wideband, low noise superconducting amplifier with high dynamic range, Nat. Phys. **8**, 623 (2012).

[30] C. Bockstiegel, J. Gao, M. R. Vissers, M. Sandberg, S. Chaudhuri, A. Sanders, L. R. Vale, K. D. Irwin, and D. P. Pappas, Development of a broadband nbtin traveling wave parametric amplifier for mkid readout, J. Low Temp. Phys. **176**, 476 (2014).

[31] C. Macklin, K. O'Brien, D. Hover, M. E. Schwartz, V. Bolkhovsky, X. Zhang, W. D. Oliver, and I. Siddiqi, A near–quantum-limited Josephson traveling-wave parametric amplifier, Science **350**, 307 (2015).

[32] A. B. Zorin, Josephson Traveling-Wave Parametric Amplifier with Three-Wave Mixing, Phys. Rev. Appl. **6**, 034006 (2016).

[33] L. Planat, A. Ranadive, R. Dassonneville, J. P. Martínez, S. Léger, C. Naud, O. Buisson, W. Hasch-Guichard, D. M. Basko, and N. Roch, A photonic crystal Josephson traveling wave parametric amplifier, arXiv:1907.10158 [quant-ph] (2019).

[34] C. Eichler and A. Wallraff, Controlling the dynamic range of a Josephson parametric amplifier, EPJ Quantum Technol. **1**, 1 (2014).

[35] X. Zhou, V. Schmitt, P. Bertet, D. Vion, W. Wustmann, V. Shumeiko, and D. Esteve, High-gain weakly nonlinear flux-modulated Josephson parametric amplifier using a squid array, Phys. Rev. B **89**, 214517 (2014).

[36] B. A. Kochetov and A. Fedorov, Higher-order nonlinear effects in a Josephson parametric amplifier, Phys. Rev. B **92**, 224304 (2015).

[37] S. Boutin, D. M. Toyli, A. V. Venkatramani, A. W. Eddins, I. Siddiqi, and A. Blais, Effect of Higher-Order Nonlinearities on Amplification and Squeezing in Josephson Parametric Amplifiers, Phys. Rev. Appl. **8**, 054030 (2017).

[38] G. Liu, T.-C. Chien, X. Cao, O. Lanes, E. Alpern, D. Pekker, and M. Hatridge, Josephson parametric converter saturation and higher order effects, Appl. Phys. Lett. **111**, 202603 (2017).

[39] N. E. Frattini, V. V. Sivak, A. Lingenfelter, S. Shankar, and M. H. Devoret, Optimizing the Nonlinearity and Dissipation of a Snail Parametric Amplifier for Dynamic Range, Phys. Rev. Appl. **10**, 054020 (2018).

[40] L. Planat, R. Dassonneville, J. P. Martínez, F. Foroughi, O. Buisson, W. Hasch-Guichard, C. Naud, R. Vijay, K. Murch, and N. Roch, Understanding the Saturation Power of Josephson Parametric Amplifiers Made From Squid Arrays, Phys. Rev. Appl. **11**, 034014 (2019).

[41] B. Abdo, K. Sliwa, L. Frunzio, and M. Devoret, Directional Amplification With a Josephson Circuit, Phys. Rev. X **3**, 031001 (2013).

[42] K. M. Sliwa, M. Hatridge, A. Narla, S. Shankar, L. Frunzio, R. J. Schoelkopf, and M. H. Devoret, Reconfigurable Josephson Circulator/Directional Amplifier, Phys. Rev. X **5**, 041020 (2015).

[43] F. Lecocq, L. Ranzani, G. A. Peterson, K. Cicak, R. W. Simmonds, J. D. Teufel, and J. Aumentado, Nonreciprocal Microwave Signal Processing with a Field-Programmable Josephson Amplifier, Phys. Rev. Appl. **7**, 024028 (2017).

[44] V. V. Sivak, S. Shankar, G. Liu, J. Aumentado, and M. H. Devoret, Josephson Array-Mode Parametric Amplifier, Phys. Rev. Appl. **13**, 024014 (2020).
[45] N. E. Frattini, U. Vool, S. Shankar, A. Narla, K. M. Sliwa, and M. H. Devoret, 3-Wave mixing Josephson dipole element, Appl. Phys. Lett. **110**, 222603 (2017).
[46] M. Hatridge, S. Shankar, M. Mirrahimi, F. Schackert, K. Geerlings, T. Brecht, K. M. Sliwa, B. Abdo, L. Frunzio, S. M. Girvin, R. J. Schoelkopf, and M. H. Devoret, Quantum back-action of an individual variable-strength measurement, Science **339**, 178 (2013).
[47] J. Koch, T. M. Yu, J. Gambetta, A. A. Houck, D. I. Schuster, J. Majer, A. Blais, M. H. Devoret, S. M. Girvin, and R. J. Schoelkopf, Charge-insensitive qubit design derived from the cooper pair box, Phys. Rev. A **76**, 042319 (2007).
[48] U. Vool, I. M. Pop, K. Sliwa, B. Abdo, C. Wang, T. Brecht, Y. Y. Gao, S. Shankar, M. Hatridge, G. Catelani, M. Mirrahimi, L. Frunzio, R. J. Schoelkopf, L. I. Glazman, and M. H. Devoret, Non-Poissonian Quantum Jumps of a Fluxonium Qubit Due to Quasiparticle Excitations, Phys. Rev. Lett. **113**, 247001 (2014).
[49] R. Fazio and H. van der Zant, Quantum phase transitions and vortex dynamics in superconducting networks, Phys. Rep. **355**, 235 (2001).
[50] N. A. Masluk, I. M. Pop, A. Kamal, Z. K. Minev, and M. H. Devoret, Microwave Characterization of Josephson Junction Arrays: Implementing a Low Loss Superinductance, Phys. Rev. Lett. **109**, 137002 (2012).
[51] T. Weißl, B. Küng, E. Dumur, A. K. Feofanov, I. Matei, C. Naud, O. Buisson, F. W. J. Hekking, and W. Guichard, Kerr coefficients of plasma resonances in Josephson junction chains, Phys. Rev. B **92**, 104508 (2015).
[52] Y. Krupko, V. D. Nguyen, T. Weißl, E. Dumur, J. Puertas, R. Dassonneville, C. Naud, F. W. J. Hekking, D. M. Basko, O. Buisson, N. Roch, and W. Hasch-Guichard, Kerr nonlinearity in a superconducting Josephson metamaterial, Phys. Rev. B **98**, 094516 (2018).
[53] P. R. Muppalla, O. Gargiulo, S. I. Mirzaei, B. P. Venkatesh, M. L. Juan, L. Grünhaupt, I. M. Pop, and G. Kirchmair, Bistability in a mesoscopic Josephson junction array resonator, Phys. Rev. B **97**, 024518 (2018).
[54] C. Hutter, E. A. Tholén, K. Stannigel, J. Lidmar, and D. B. Haviland, Josephson junction transmission lines as tunable artificial crystals, Phys. Rev. B **83**, 014511 (2011).
[55] B. Yurke, M. L. Roukes, R. Movshovich, and A. N. Pargellis, A low-noise series-array Josephson junction parametric amplifier, Appl. Phys. Lett. **69**, 3078 (1996).
[56] P. Lähteenmäki, G. S. Paraoanu, J. Hassel, and P. J. Hakonen, Dynamical Casimir effect in a Josephson metamaterial, Proc. Natl. Acad. Sci. **110**, 4234 (2013).
[57] D. H. Slichter, Ph.D. thesis, School UC Berkeley, (2011).
[58] L. Grünhaupt, U. von Lüpke, D. Gusenkova, S. T. Skacel, N. Maleeva, S. Schlör, A. Bilmes, H. Rotzinger, A. V. Ustinov, M. Weides, and I. M. Pop, An argon ion beam milling process for native alox layers enabling coherent superconducting contacts, Appl. Phys. Lett. **111**, 072601 (2017).
[59] X. Wu, J. L. Long, H. S. Ku, R. E. Lake, M. Bal, and D. P. Pappas, Overlap junctions for high coherence superconducting qubits, Appl. Phys. Lett. **111**, 032602 (2017).
[60] F. Lecocq, I. M. Pop, Z. Peng, I. Matei, T. Crozes, T. Fournier, C. Naud, W. Guichard, and O. Buisson, Junction fabrication by shadow evaporation without a suspended bridge, Nanotechnology **22**, 315302 (2011).
[61] A. Kou, W. C. Smith, U. Vool, I. M. Pop, K. M. Sliwa, M. Hatridge, L. Frunzio, and M. H. Devoret, Simultaneous Monitoring of Fluxonium Qubits in a Waveguide, Phys. Rev. Appl. **9**, 064022 (2018).
[62] N. F. Ramsey, A molecular beam resonance method with separated oscillating fields, Phys. Rev. **78**, 695 (1950).
[63] J. Heinsoo, C. K. Andersen, A. Remm, S. Krinner, T. Walter, Y. Salathé, S. Gasparinetti, J.-C. Besse, A. Potočnik, A. Wallraff, and C. Eichler, Rapid High-Fidelity Multiplexed Readout of Superconducting Qubits, Phys. Rev. Appl. **10**, 034040 (2018).
[64] V. V. Sivak, N. E. Frattini, V. R. Joshi, A. Lingenfelter, S. Shankar, and M. H. Devoret, Kerr-Free Three-Wave Mixing in Superconducting Quantum Circuits, Phys. Rev. Appl. **11**, 054060 (2019).
[65] Qkit – A quantum measurement suite in python.
[66] C. Paul, *Analysis of Multiconductor Transmission Lines*, Wiley Series in Microwave and Optical Engineering (Wiley, Hoboken, New Jersey, 1994).
[67] D. Pozar, *Microwave Engineering* (Wiley, Hoboken, New Jersey, 2011), 4th ed.
[68] S. E. Nigg, H. Paik, B. Vlastakis, G. Kirchmair, S. Shankar, L. Frunzio, M. H. Devoret, R. J. Schoelkopf, and S. M. Girvin, Black-Box Superconducting Circuit Quantization, Phys. Rev. Lett. **108**, 240502 (2012).
[69] J. Gambetta, A. Blais, D. I. Schuster, A. Wallraff, L. Frunzio, J. Majer, M. H. Devoret, S. M. Girvin, and R. J. Schoelkopf, Qubit-photon interactions in a cavity: Measurement-induced dephasing and number splitting, Phys. Rev. A **74**, 042318 (2006).